Palmitic Acid Accumulation Activates Fibroblasts and Promotes Matrix Stiffness in Colorectal Cancer

Shenghe Deng[1], Jun Wang[2], Falong Zou[2], Denglong Cheng[2], Mian Chen[2], Junnan Gu[2], Jianguo Shi[3], Jia Yang[3], Yifan Xue[2], Zhenxin Jiang[2], Le Qin[2], Fuwei Mao[2], Xiaona Chang[4], Xiu Nie[4], Li Liu[5], Yinghao Cao[6,7], and Kailin Cai[2]

ABSTRACT

Obstructions can occur during any stage of colorectal cancer and correspond with poor prognosis. Obstructive colorectal cancer (OCRC) is harder and exhibits increased tumor budding and proliferation of myofibroblasts compared with non-obstructive colorectal cancer, suggesting that the occurrence of obstruction may be related to extracellular matrix (ECM) remodeling. In this study, we found that colorectal cancer and OCRC samples differed substantially in ECM composition, specifically in collagen (newly formed and mature) and proteoglycans (including glycosaminoglycan, hyaluronic acid, and chondroitin sulfate). OCRC also exhibited considerable changes in ECM biomechanics and collagen arrangement. Interestingly, OCRC samples presented a notable increase in matrix cancer-associated fibroblasts (mCAF). The abundance of mCAFs correlated with the accumulation of palmitic acid (PA), and high concentrations of PA increased the secretion of ECM-related proteins by mCAFs. Additionally, PA did not directly affect normal fibroblasts but rather activated the NF-κB pathway in tumor cells to stimulate secretion of CSF1, TGFβ1, and CXCL8, which promoted the activation of normal fibroblasts into mCAFs and exacerbated ECM stiffening. Drug screening with a natural compound library identified vanillylacetone as a potential inhibitor of PA-induced cytokine secretion and ECM stiffening. These findings highlight intratumoral PA accumulation as a key mechanism driving ECM alterations and OCRC progression and suggest that targeting this axis may be useful for treating patients with colorectal cancer with risk of obstruction.

Significance: Palmitic acid accumulation activates the NF-κB pathway in colorectal cancer cells to promote cytokine secretion that facilitates the generation of matrix cancer-associated fibroblasts, driving extracellular matrix remodeling and development of obstructions.

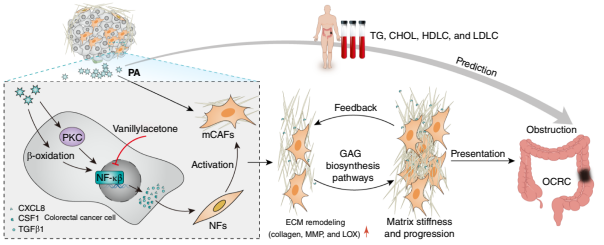

Introduction

Colorectal cancer is the third most common cancer and the second leading cause of cancer-related death, and up to 33% of patients with colorectal cancer present with symptoms such as obstruction, perforation, and bleeding requiring emergency surgical intervention (1, 2). If obstructive colorectal cancer (OCRC) is not diagnosed and treated promptly, the mortality rate can reach to 30% (3). Therefore, OCRC is an important challenge that needs to be urgently addressed.

Although many clinical studies have reported the poor prognosis of OCRC (4, 5), the related mechanism remains unclear. Extracellular matrix (ECM) remodeling is associated with the pathologic phenotype of tumors and facilitates tumor progression. The constitution, density, and mechanical properties of the remodeled ECM are substantially altered during tumorigenesis and metastasis and are closely related to these processes (6–8). OCRC may be associated with ECM remodeling, as significant interfibrillar responses have been detected in the plasma membrane of OCRC tissue (9, 10). Compared with colorectal cancer, OCRC exhibits increased tumor budding and proliferation of myofibroblasts expressing high levels of alpha smooth muscle actin (αSMA), leading to increased stromal fibrosis (11). Clinically, we have observed that excised OCRC samples are harder than colorectal cancer samples. Therefore, the occurrence of obstruction may be related to the specificity of ECM remodeling.

[1]Department of General Surgery, Union Hospital, Tongji Medical College, Huazhong University of Science and Technology, Wuhan, China. [2]Department of Gastrointestinal Surgery, Union Hospital, Tongji Medical College, Huazhong University of Science and Technology, Wuhan, China. [3]Department of Gastrointestinal Surgery, The Central Hospital of Wuhan, Tongji Medical College, Huazhong University of Science and Technology, Wuhan, China. [4]Department of Pathology, Union Hospital, Tongji Medical, Huazhong University of Science and Technology, Wuhan, China. [5]Department of Epidemiology and Biostatistics, School of Public Health, Tongji Medical College, Huazhong University of Science and Technology, Wuhan, China. [6]Department of Digestive Surgical Oncology, Cancer Center, Union Hospital, Tongji Medical College, Huazhong University of Science and Technology, Wuhan, China. [7]Clinical Imaging Research Centre, Centre for Translational Medicine, Yong Loo Lin School of Medicine, National University of Singapore, Singapore, Singapore.

S. Deng, J. Wang, F. Zou, and D. Cheng contributed equally to this article.

Corresponding Authors: Yinghao Cao, Department of Digestive Surgical Oncology, Cancer Center, Union Hospital, Tongji Medical College, Huazhong University of Science and Technology, Wuhan 430022, China. E-mail: 2022XH0021@hust.edu.cn; and Kailin Cai, Gastrointestinal Surgery, Union Hospital, Tongji Medical College, Huazhong University of Science and Technology, Wuhan 430022, China. E-mail: caikailin@hust.edu.cn

Cancer Res 2025;85:1784–802

doi: 10.1158/0008-5472.CAN-24-2892

ECM generation, dynamic homeostasis, and remodeling depend on tumor and mesenchymal stromal cells. Cancer-associated fibroblasts (CAF), major cellular components of the tumor microenvironment (TME), can degrade ECM components and release growth factors and cytokines to promote ECM production, establishing a new ecological niche different from that of the physiologic ECM (12). However, the roles and mechanisms of cell-to-cell signaling within the TME, particularly in ECM remodeling and OCRC development, remain poorly understood. Biochemical and physical signals from the ECM influence therapy outcomes (13). Therefore, finding effective therapeutic agents that target the ECM has practical clinical implications for OCRC.

To enhance our understanding of OCRC, we examined and validated the mechanisms leading to OCRC, by comparing OCRC and colorectal cancer cases in terms of their clinical characteristics and ECM constitution and structure. Multiomics analysis and drug screening were used. We expect that these findings will reveal potential therapeutic targets for the comprehensive treatment of colorectal cancer and elucidate the mechanisms of OCRC progression.

Materials and Methods

Human colorectal cancer tissue specimens, clinicopathologic characteristics, and ethical statement

Patients with colorectal cancer in Wuhan Union Hospital from 2010 to 2016 were included according to the inclusion and exclusion criteria. The inclusion criteria were as follows: (i) patients with colorectal cancer confirmed by pathology (UICC Colorectal Cancer Staging Manual, seventh edition); (ii) patients who underwent resection for colorectal cancer; and (iii) patients who were diagnosed preoperatively with or without colorectal obstruction. The exclusion criteria were as follows: (i) patients with distant metastasis or invasion of adjacent organs; (ii) patients who underwent R1/R2 resection; (iii) patients who experienced a tumor rupture; (iv) patients with severe cardiopulmonary disease or mental disorders; and (v) patients who did not sign the informed consent.

A total of 1,470 patients were included and divided into an obstruction group (OCRC, $n = 198$) and a nonobstruction group (colorectal cancer, $n = 1{,}272$) on the basis of the presence or absence of colorectal obstruction. Age, sex, body mass index (BMI), tumor location, tumor size, tumor–node–metastasis (TNM) stage, degree of differentiation, perineural invasion (PNI), vascular invasion, and circumferential resection margin data were collected and followed up at later dates. To further explain the difference in survival between patients with OCRC and colorectal cancer, we performed propensity score matching (PSM) analysis. The combined selection of possible variables associated with prognostic factors in patients with cancer included age, sex, degree of differentiation, T stage, N stage, M stage, tumor site, tumor size, adjuvant chemotherapy, radiotherapy, carcinoembryonic antigen, CA199, CA125, and CA724, which were matched by the one-to-one best matching method on the basis of the logic of a propensity score within 0.037 calipers. The standardized difference was used to evaluate the balance of the matched covariates, the acceptable standardized difference was considered less than 10%, and 150 pairs of clinical cases were eventually included.

Paraffin-embedded tissue samples were collected from the enrolled patients. Additionally, fresh colorectal cancer tissue samples were collected and preserved separately through paraffin-embedding and freezing at −80°C. All the collected tissues were confirmed to be colorectal cancer tissues through postoperative pathologic examination. None of the patients received adjuvant chemotherapy before surgery. The study protocol was reviewed and approved by the Ethics Committee and Institutional Review Committee of Wuhan Union Hospital (nos. 2018-S377 and 2024-0830). All patients provided written informed consent, and all procedures performed in studies involving human participants were accordance with the Helsinki Declaration.

Movat pentachrome staining

The staining process was carried out according to the instructions of Movat-Russell Modified Pentachrome Stain Kit (G3701, Solarbio). Briefly, after deparaffinization, the tissue sections were treated with a fixative solution. After the dewaxed slices were treated with fixation solution, they were successively subjected to alcian blue staining, an alkaline ethanol solution, hematoxylin staining solution, and saffron staining solution. The sections were subsequently treated with phosphotungstic acid solution and saffron staining solution. Finally, the tissue sections were dehydrated and sealed with neutral gum.

Masson staining

Masson staining was performed according to the instructions of Masson's Trichrome Stainless Kit (G1340-7, Solarbio). In brief, the tissue sections were dehydrated and then sequentially treated with potassium dichromate, iron hematoxylin, Ponceau acid fuchsin, phosphomolybdate aqueous solution, and aniline blue dye staining solutions, and the tissue sections were sealed with neutral gum after dehydration. The collagen volume fraction was calculated from 3 to 5 randomly selected fields per section with ImageJ (NIH).

Picrosirius red staining and polarizing light microscopy

Picrosirius red staining was performed according to the instructions of Picro Sirius Red Kit (MM1004, MaoKang Biotechnology). After the slices were dewaxed, they were immersed in Sirius scarlet dye, dehydrated with anhydrous ethanol, cleared with xylene, and finally sealed with neutral gum. Changes in mature collagen fibers (red/orange) and newly formed collagen fibers (yellow/green) were recorded. To detect red, orange, yellow, and green fibers, the images were transferred to the HSV color space. The percentages of red (0–9,230–256), orange (10–38), yellow (39–51), and green (52–128) pixels in each image were analyzed with ImageJ software. The angles of the collagen fibers were measured with the angle tool in ImageJ, and all the angles were referenced to a horizontal line. Three images were analyzed for each tissue, and at least 20 collagen fiber angles were measured per image to calculate the alignment index (AI). $AI = 0$ refers to a random orientation, and $AI = 1$ describes fully aligned fibers (8).

Safranin O-fast green staining

Safranin fast green staining was carried out according to the instruction manual of the Safranin O-fast green cartilage staining kit (G1371, Solarbio). The paraffin sections were dewaxed, dipped in Weigert staining solution, fast green staining solution, and safranin O stain, dehydrated, and sealed with neutral gum.

Oil Red O staining

Oil Red O staining was carried out according to the instruction manual of Oil Red O Staining Kit (C0157S, Beyotime). The frozen sections were dried at room temperature, sequentially placed into prepared Oil Red O staining solution, soaking solution, and hematoxylin

staining solution for staining, placed in hematoxylin blue-returning solution, and sealed with glycerin–gelatin.

Atomic force microscopy

Frozen cryosectioned tissue samples were thawed and washed with PBS to remove residues of Tissue Tek. The samples were subsequently examined at room temperature using an atomic force microscopy (AFM) device (MFP3D-Bio, Asylum Research). Using a sphere-tip cantilever with a nominal tip radius of 2 μm, a scan area of 50 × 50 μm^2 was selected. The velocity and maximum force of the force–indentation curve were 20 μm/seconds and 5 nN, respectively. Each force–distance curve was analyzed by the Hertz model (14–16). Each tissue analysis was repeated three times, and the average Young modulus was calculated. Statistical significance was determined with Student *t* test.

Raman microspectroscopy

All measurements are made using a custom-built inverse Raman microspectrometer equipped with a near-IR laser diode (85 mW laser power, 784 nm; ref. 8). The total accumulation time of each spectrum was 100 seconds when a water immersion objective lens (60 minutes NA1.2) was used. The collagen-rich regions selected from serial tissue sections on the basis of the results of tissue staining were identified by brightfield microscopy. For each tissue sample, two sections were analyzed, and the mean values were calculated. Raman wavenumbers, including C–C stretching vibrations (777, 819, 860, and 942 cm^{-1}), were observed, 860/879 cm^{-1} (proline/hydroxyproline) values were calculated, the area of the C-O peak at 1,128 cm^{-1} was used to assess the glycosaminoglycan (GAG) content, and the protein-to-GAG ratio was assessed by the Raman signal ratio at 1,250/1,341 cm^{-1}.

Cell lines and cell culture

The human colon cancer cell lines LoVo (cat. #CCL-229, RRID: CVCL_0399) and SW480 (cat. #CCL-228, RRID: CVCL_0546) and human umbilical vein endothelial cells (HUVEC, CRL-4053, RRID: CVCL_9Q53) were purchased from the ATCC. The mouse colon cancer cell lines CT26 (SCSP-523) and MC38 (SCSP-5431) were obtained from the National Collection of Authenticated Cell Cultures. These cell lines and primary CAFs were cultured in DMEM (No. C11995500BT, Gibco) supplemented with high glucose, 10% FBS (no. 10099141, Gibco), and 1% penicillin/streptomycin. The cells were cultured at 37°C, with 5% CO_2 and 95% air. All cell lines were tested for *Mycoplasma* contamination every 6 months using EZ-PCR Mycoplasma Test Kit (Biological Industries). Cell lines are subcultured every 2 or 3 days, and no cell line was used for more than 15 passages after thawing from frozen stocks.

Isolation of primary CAFs and normal fibroblasts and conditioned medium collection

Fresh colorectal adenocarcinoma and adjacent normal tissues were cleaned 4 to 6 times with sterile PBS containing 3% penicillin/streptomycin/amphozone and cut into 1 × 1 × 1 mm^3 pieces with scissors. Digestion was then performed at 37°C with 2% collagenase IV (C4-BIOC, Sigma-Aldrich), 1% hyaluronidase (1141MG100, BioFroxx), and DNA I enzyme (1121MG010, BioFroxx) for 4 to 6 hours. After digestion, the mixture was filtered through a 40-micron mesh (BD Falcon) and centrifuged. Red blood cells were removed from the red blood cell lysis buffer and cultured in medium. After successful cell expansion, αSMA and vimentin were used as markers for immunofluorescence staining identification (17).

For conditioned medium (CM) analysis, the cells were collected and inoculated into six-well plates for culture. When the cells reached 90% confluence, the medium was replaced with fresh F12 medium without serum, and the culture was continued for 24 hours. The CM was collected, filtered, and stored at −80°C.

FlexCell cyclic tensile strain

Primary CAFs were inoculated in BioFlex six-well plates (FlexCell Int.) at an initial cell density of 5 × 10^4 cells/well. After the cell density reached 70 to 80%, the medium was replaced with fresh medium. The CAFs were subsequently placed in the FlexCell Tension Plus FX-5000 system (FX-5000, FlexCell) for cyclic stretching for 48 hours (0.5 Hz, 15% deformation). The control group consisted of CAFs cultured on BioFlex plates without cyclic stretching. For CM collection, the medium was changed to serum-free medium for cyclic stretching for 48 hours.

Western blot, dot blot, IHC staining, immunofluorescence staining, and tissue multiplex immunofluorescence staining

Tissues or cells were lysed on ice with radioimmunoprecipitation assay lysis buffer containing 1% protease and phosphatase inhibitors. The cell lysate products were centrifuged (4°C, 12,000 rpm, 15 minutes), and the supernatant was collected. The protein content was determined with a bicinchoninic acid assay. The obtained protein was added to 5× loading buffer, heated at 95°C for 10 minutes, and used for Western blot analysis (17). For the dot blot assay, the obtained tissue or protein lysate was directly applied to a nitrocellulose blotting membrane, which was subsequently dried at 37°C. The membrane was then blocked with 5% skim milk powder, and subsequent procedures were consistent with those of Western blotting. For the IHC staining assay, the paraffin-embedded samples were sectioned and treated with H_2O_2 and nonspecific antigen blocking, and the target antibody was added and incubated at 4°C overnight, followed by incubation with the secondary antibody. The signals were detected using a DAB staining kit (DA1016, Solarbio). For the IHC staining analysis, five visual fields were randomly selected from each section. The integrated optical density/area value of each visual field was calculated with ImageJ, and the average value was used for comparative analysis. The immunofluorescence and tissue multiplex immunofluorescence staining methods for tissue or cells were similar but required incubation under dark conditions and observation by fluorescence microscopy or confocal microscopy after 4′,6-diamidino-2-phenylindole (DAPI; C1005, Beyotime) staining, and the cell density was calculated with QuPath software. The detailed antibody information used in this experiment is shown in Supplementary Table S1.

ELISA

The collected CM and cell supernatants and the serum were assayed for concentrations of the corresponding indicators using an ELISA kit (Ruixinbio) according to the instructions. All samples were tested three or more times. The absorbance (optical density value) was determined with an enzyme-labeled instrument at a wavelength of 450 nm, and the concentration of the target protein in each sample was calculated according to the standard curve.

Cell Counting Kit-8 cell proliferation assay

LoVo and SW480 cell lines were treated with different CMs containing 10% FBS, with five replicates in each group. Cell

Counting Kit-8 (CCK-8) solution (C0038, Beyotime) was added to each well, which contained 2,000 cells. The cells were incubated at 37°C for 3 hours, and the absorbance was measured at 450 nm using an enzyme marker instrument. The data were monitored continuously for 3 to 5 days and processed with GraphPad Prism V8.0 software (GraphPad Software Inc.).

Transwell assay

LoVo and SW480 cells were cultured in 24-well transwell plates with 8.0-μm pores (Corning Costar) with/without precoated Matrigel (BD; diluted 1:1). Colorectal cancer cells (LoVo and SW480; 3×10^4) were plated in the top compartment. After 24 hours of culture, the membranes were collected and stained with a crystal violet solution (G1064, Solarbio). A cotton swab was used to remove cells that did not migrate or invade through the pores. The migrating and invading cells in five different fields were counted and photographed under a microscope.

Coculture system and 3D culture assay

For the colorectal cancer cell coculture system with CAFs/normal fibroblasts (NF), CMs from different CAF treatments were collected, and different CMs at a 10% concentration were cultured with colorectal cancer/CAF/NF cells separately according to the experimental requirements. Alternatively, a cell coculture six-well plate was used, with the two cell types plated in the upper and lower chambers according to the experimental requirements to observe the cell interactions.

For 3D culture, 150 μL of Matrigel was spread on a 24-well cell culture plate and incubated at 37°C for 10 minutes to solidify. Colorectal cancer cells were resuspended in CM containing 10% FBS for a final concentration of 0.5×10^5 cells/mL, and 150 μL of cell suspension with 5 μL of Matrigel was added to the abovementioned 24-well plate. After solidification, the cells were incubated with CM containing 10% FBS, and the cell status was observed daily and photographed by phase-contrast microscopy.

Wound healing assay

LoVo and SW480 cells were inoculated in six-well culture plates. When the cell confluence reached 90%, a 200-μL sterile micropipette was used to make wounds. After incubation with CM for 0 and 24 hours, the gap between the two wound edges was measured. The mobility was calculated as (initial area−final area)/initial area (17).

Tube formation assay

A 96-well cell culture plate was selected, and 50 μL of Matrigel was spread in each well and placed in an incubator at 37°C for 10 minutes to solidify. Cell suspensions were made by applying different CMs containing 10% FBS to HUVECs (CRL-4053, RRID: CVCL_9Q53), with 2×10^4 cells added to each well, and tube formation was observed under a microscope after 6 hours. Statistical software was used for analysis with ImageJ.

RNA extraction and qRT–PCR

Total RNA was extracted from tissues and cells with TRIzol reagent (No. 15596026, Invitrogen) and RNApure TissueCell Kit (CW0584S, CWBIO), and the RNA concentration was determined using a spectrophotometer. The RNA samples (1 μg) were reverse transcribed into cDNA using a reverse transcription kit (R323-01, Vazyme). Super SYBR Green Kit (R223-01, Vazyme) was used to perform qRT–PCR. Each sample was tested at least three times, and the average value was used for data analysis. The primer sequences for these genes are listed in Supplementary Table S2.

Reactive oxygen species detection

A reactive oxygen species (ROS) assay kit (S0033S, Beyotime) was used for this experiment. DCFH-DA was diluted with serum-free medium at a concentration of 1:1,000. The medium was removed after 24 hours of treatment with palmitic acid (PA), the diluted serum-free medium containing DCFH-DA was added, the cells were incubated in the dark for 20 minutes, and the medium was removed, followed by three washes with PBS. Hoechst dye was diluted to a concentration of 1:1,000, and the nuclei were stained for approximately 7 minutes. Photographs were taken under a fluorescence microscope.

Xenotransplantation, orthotopic and lung metastasis colorectal cancer model

Nude mice were randomly divided into three groups. In the intervention group, CAFs + colorectal cancer cells were injected into the tail vein at the ratio of 1:1 (cells volume 3×10^6, respectively), whereas in the control group, only colorectal cancer cells were injected. CAFs in the intervention group were derived from human OCRC and colorectal cancer tissues. After 1 month of normal diet, lung tissue was collected. Hematoxylin and eosin staining was performed on the lung tissue, and metastatic nodules of lung tissue were calculated.

C57BL/6, BALB/c and $APC^{min/+}$ mice were purchased and divided into experimental and control groups. The mice in the experimental group were fed a diet containing 10% PA, and the mice in the control group were fed a regular diet with an equal amount of total energy. Two weeks later, C57BL/6 and BALB/c mice were inoculated with 2×10^6 MC38 (SCSP-5431) and CT26 (SCSP-523) cells in the right groin, and the dietary treatment was continued. The subcutaneous tumor volume was recorded every 3 days after tumor formation, and the tumor volume was calculated according to the formula $(L \times W^2)/2$. The subcutaneous tumors were excised and weighed approximately 3 to 4 weeks after tumor formation. For the orthotopic tumor model, after 14 weeks of feeding, the number of *in situ* tumors was observed in $APC^{min/+}$ mice ages 4 weeks.

In the validation experiments with vanillylacetone (S2371, Selleck), C57BL/6 and BALB/c mice were used to establish subcutaneous tumors in a manner similar to the previously described method. These mice were divided into control, PA, and PA + vanillylacetone groups. The dose of vanillylacetone was 25 mg/kg, which was administered once every 2 days for 2 to 3 weeks. The volume and weight of the subcutaneous tumors were then assessed. All the animal studies were conducted in accordance with the guidelines approved by the Animal Experimental Ethics Committee of Tongji Medical College, Huazhong University of Science and Technology, China (Institutional Animal Care and Use Committee, no. 2022-3049).

Digital spatial profiling

Paraffin-embedded slides prepared from OCRC, colorectal cancer, and normal tissues were subjected to immunofluorescent antibody staining to identify tissue morphology: CAFs (anti–αSMA antibody), epithelial cells (anti-PanCK antibody), and nuclei (Syto13 stain). The stained slides were loaded into the GeoMx instrument for scanning. Multiple circular regions of interest (ROI) with a diameter of 500 μm were selected for each tissue core. Oligonucleotide tags within these ROIs were then excised under

ultraviolet light irradiation and collected for digital quantification. Finally, the data were analyzed to interpret the detailed expression profiles within these discrete ROIs (18). The differential expression results of SMA-positive cells in OCRC, colorectal cancer, and normal tissues are shown in Supplementary Excel S1.

Digital RNA sequencing

Total RNA samples were prepared with TRIzol reagent (no. 15596026, Invitrogen). The samples were analyzed on agarose gels for RNA integrity and DNA contamination, and the purity of the RNA was determined using a nanospectrophotometer. The RNA concentration was accurately quantified using a Qubit 2.0 fluorometer, and RNA integrity was accurately detected using an Agilent 2100 bioanalyzer. The library was constructed using Illumina NEBNext Ultra RNA Library Prep Kit, and the library was initially quantified with using the Qubit 2.0 fluorometer and diluted to 1.5 ng/μL. The insert size of the library was checked by an Agilent 2100 bioanalyzer, and the effective concentration of the library was accurately quantified by qRT–PCR after the insert size met expectations. The libraries that passed the test were pooled according to the effective concentration and the target downstream data volume and then sequenced by Illumina.

Nontargeted metabolomics

The sample, which was previously stored at −80°C, was thawed on ice. After thawing, the sample was homogenized with a grinder at 30 Hz for 20 seconds. To a 20 mg ground sample, 400 μL of a methanol solution (7:3, v/v) containing an internal standard was added, and the mixture was shaken at 1,500 rpm for 5 minutes. The sample was then allowed to rest on ice for 15 minutes before being centrifuged at 12,000 rpm for 10 minutes at 4°C. Subsequently, 300 μL of the supernatant was collected and chilled at −20°C for 30 minutes, followed by another centrifugation at 12,000 rpm for 3 minutes at 4°C. A 200 μL aliquot of the resulting supernatant was used for LC–MS analysis. All the samples were processed with the LC–MS system according to the instrument protocols. The analytical conditions were as follows: UPLC with a Waters ACQUITY UPLC HSS T3 C18 column (1.8 μm, 2.1 mm × 100 mm); the column temperature was set to 40°C; the flow rate was 0.4 mL/minutes; the injection volume was 2 μL; and the solvent system was comprised of water (0.1% formic acid) and acetonitrile (0.1% formic acid) in a gradient program that started at 95:5 v/v at 0 minute, shifted to 10:90 v/v at 11.0 minutes, was maintained at 10:90 v/v at 12.0 minutes, returned to 95:5 v/v at 12.1 minutes, and held at 95:5 v/v until 14.0 minutes. Screening for differentially abundant metabolites between groups was conducted on the basis of variable importance projection ≥1, P value < 0.05, and a fold change ≥1.2. The relative contents of different metabolites were standardized. The analysis of nontargeted metabolomic differences between OCRC and colorectal cancer tissues is shown in Supplementary Excel S2.

Detection of PA content in tumors

One milliliter of extraction solution (MeOH:CH2Cl2:hexane = 1:1:1 v/v/v, including internal standard stearic acid-d3 40 ng/mL) was added to the tumor samples for every 100 mg of tissue, and the mixture was homogenized at 5,500 rpm for 30 to 45 seconds and centrifuged at 4°C at 12,000 rpm for 10 minutes. The supernatant was concentrated under vacuum in a rotary drying apparatus for 2 to 3 hours and redissolved in 100 μL of methanol, and the derivatization reaction was performed. Every 100 μL sample was mixed with 50 μL of 0.2 mol/L 3-NPH and 50 μL of 0.12 mol/L EDC on ice at 40°C for 60 minutes. The sample was subsequently centrifuged at 10,000 rpm at 4°C for 10 minutes, after which, 80 μL was absorbed for machine detection. The instrument used was an ultra-performance liquid chromatography (Waters ACQUITY) coupled with a triple-quadrupole tandem mass spectrometer (AB Sciex 5500). The chromatographic column used was an ACQUITY Premier HSS T3 column (1.8 μm, 2.1 × 100 mm). Mobile phase A was 0.1% formic acid, and mobile phase B was acetonitrile/isopropanol = 5:1. One hundred milligrams of each tumor tissue sample was precisely weighed, and 1 mL of extraction mixture (MeOH:CH_2Cl_2:hexyl hydride = 1:1:1 v/v/v, containing 40 ng/mL internal standard stearic acid-d3) was added.

Statistical analysis

Overall survival (OS) and disease-free survival (DFS) were analyzed using the Kaplan–Meier analysis. The results were presented as the mean ± SD. The two groups were compared using an unpaired Student t test or the Mann–Whitney U test. Comparison of variables between groups was performed using the ANOVA or Kruskal–Wallis test. R software (4.1.0) was used for all statistical analyses, and the statistical significance was as follows: ns, not significant; *, $P < 0.05$; **, $P < 0.01$; ***, $P < 0.001$; ****, $P < 0.0001$.

Data availability

The data generated in this study are available upon request from the corresponding author (Kailin Cai, caikailin@hust.edu.cn). The RNA sequencing (RNA-seq) data generated in this study are publicly available in the NCBI Sequence Read Archive database at PRJNA1152877, PRJNA1151631, PRJNA1153440, and PRJNA1180984.

Results

OCRC and colorectal cancer differed substantially in clinicopathology, with poorer prognoses in OCRC

We analyzed the clinicopathologic characteristics of 1,470 patients with malignant colorectal tumors (OCRC, $n = 198$; colorectal cancer, $n = 1,272$). OS and DFS were significantly poorer in patients with OCRC than in those with colorectal cancer (Supplementary Fig. S1A). These groups also differed notably in terms of age, BMI, TNM stage, and PNI (Supplementary Fig. S1B). Using PSM analysis, we matched 150 pairs of patients with OCRC and colorectal cancer for further analysis. Compared with the colorectal cancer group, the OCRC group had a significantly worse prognosis. The BMI and PNI were significantly higher for patients with OCRC than for those with colorectal cancer, suggesting that OCRC has worse clinicopathologic characteristics and may be associated with metabolic abnormalities (Supplementary Fig. S1C and S1D).

OCRC and colorectal cancer differed substantially in ECM constitution, biomechanics, and collagen characteristics

Clinicopathologically, OCRC tissue exhibited greater hardness and luminal contraction, indicating invasive growth. We therefore analyzed the ECM constitution and structure in OCRC and colorectal cancer. PSM identified 10 pairs of OCRC and colorectal cancer tissue samples at TNM stage III, including three pairs of matched normal tissue samples. Movat pentachrome and Masson staining were used to assess the ECM constitution and fiber content of normal colon and tumor tissue. Compared with normal tissue, colorectal cancer and OCRC tissues presented an altered ECM constitution, with a marked presence of collagen fibers. Compared with colorectal cancer tissue, OCRC tissue presented a significantly

greater increase in collagen fiber content (**Fig. 1A** and **B**; Supplementary Fig. S2A and S2B). Given the disrupted arrangement of tumor tissue relative to normal tissue, we evaluated its elastic properties by analyzing its collagen structure. Collagen-rich areas of the tissue were identified via Movat pentachrome and Masson staining. The AFM force maps for each region revealed that the elastic properties of the collagen-enriched ECM of OCRC and colorectal cancer tissues differed from those of normal tissues. The mean *E*-modulus of the collagen-rich regions was significantly greater in OCRC and colorectal cancer tissues than in normal tissues, with a notably elevated mean *E*-modulus in OCRC tissues (**Fig. 1C** and **D**; Supplementary Fig. S2C).

C–C stretching and proline signals in Raman spectra are markers for confirming the presence of collagen (19, 20). Therefore, we conducted Raman microspectroscopy to elucidate the biomolecular constitution of the collagen-rich ECM in OCRC and colorectal cancer tissues. The C–C stretch vibration intensity was significantly lower in the OCRC group than in the colorectal cancer group ($n = 10$) at 777, 860, 879, and 942 cm^{-1}, suggesting a greater abundance of collagen in the OCRC tissue (**Fig. 1E**; Supplementary Fig. S2D). The proline-to-hydroxyproline ratio (860/879 cm^{-1}) was significantly lower in the OCRC group than in the control group, indicating elevated hydroxyproline content in the collagen-rich OCRC tissue (**Fig. 1F**).

Raman spectroscopy can be used to evaluate the GAG content by evaluating the peak intensities of carbohydrate and glycan vibrations (21). Compared with the colorectal cancer tissue, the OCRC tissue presented significantly greater carbohydrate-specific Raman signals, particularly at 1,128 cm^{-1} (Supplementary Fig. S2D). The GAG:-protein ratio in the ECM (1,341 cm^{-1}: 1,250 cm^{-1}) was notably greater in the OCRC group than in the control group, indicating elevated GAG content in the OCRC ECM (**Fig. 1G**). GAGs are categorized as chondroitin sulfate, heparan sulfate, or hyaluronic acid (HA) based on their core disaccharide structure. IHC staining revealed that the HA receptor CD44 was significantly more abundant in OCRC tissue than in colorectal cancer tissue (Supplementary Fig. S2E). Safranin O/fast green staining revealed that the chondroitin sulfate content was substantially greater in the ECM of OCRC tissue than in that of colorectal cancer tissue (Supplementary Fig. S2F). The OCRC and colorectal cancer tissue therefore differed significantly in the constitution of their ECMs.

We systematically analyzed the collagen fiber structure within each group ($n = 15$). Via Picrosirius red staining and polarization microscopy, type III collagen fibers were found to be predominant in tumor tissue, whereas type I collagen fibers were predominant in the submucosa of normal tissue (**Fig. 1H**). Both newly formed (yellow/green) and mature (red/orange) collagen fibers were significantly more abundant in OCRC tissue than in colorectal cancer tissue (**Fig. 1I**). Analysis of the AI revealed a more directional arrangement of collagen in the OCRC ECM. The amide signal (1,250 and 1,666 cm^{-1}) in the Raman spectra, indicative of collagen orientation, confirmed a more regular and potentially remodeled collagen fiber network in OCRC tissue (Supplementary Fig. S2G and S2H).

OCRC and colorectal cancer differed in stromal cells and the TME, with significantly more matrix CAFs in OCRC

The altered physicochemical properties of the ECM are believed to be closely associated with the occurrence of OCRC, influencing microvessels, lymphatic vessel formation, the immune microenvironment, and tumor progression (22). CAFs are critical cellular components of the tumor stroma and are implicated in OCRC development (23, 24). Consequently, we compared the stromal constitution of OCRC and colorectal cancer, focusing primarily on CAFs (αSMA), epithelial cells (EMA), microvessels (CD34), microlymphatics (D2-40), and the immune component of the TME. We analyzed 150 pairs of paraffin-embedded tissue samples from patients with OCRC and colorectal cancer and conducted IHC staining on 107 pairs, revealing markedly elevated CAF content, microvessel density (MVD), and microlymphatic vessel density (MLD) in the OCRC tissue. Semiquantitative analysis of αSMA and EMA suggested a greater degree of tumor epithelial–mesenchymal transition (EMT) in OCRC tissues than in colorectal cancer tissues. Through IHC staining ($n = 77$) and tissue multiplex immunofluorescence ($n = 10$), we confirmed that there were significant differences in the infiltration content of $CD4^+$ T cells, $CD8^+$ T cells, M0 macrophages (CD68), M2 macrophages (CD163), and neutrophils (CD11b) in the OCRC and colorectal cancer TMEs (**Fig. 1J**; Supplementary Figs. S2I and S3A–S3C). OCRC and colorectal cancer therefore differed substantially in the composition and structure of the ECM as well as in the immune microenvironment, and notably, CAFs were significantly more abundant in OCRC tissue, which correlated strongly with the altered physicochemical properties of the ECM.

To further elucidate the CAF subtypes, we used digital spatial profiling (DSP) technology for the quantitative analysis of αSMA-positive CAFs and NFs in OCRC (ROI = 10), colorectal cancer (ROI = 8), and normal (ROI = 6) tissues (**Fig. 2A**). Comparative studies of OCRC, colorectal cancer, and normal tissues revealed pronounced upregulation of genes coding collagen, matrix metalloproteinases (*MMP*), lysyl oxidase (*LOX*), and *TGFβ1* in αSMA–positive CAFs from OCRC tissues. Additionally, markers of matrix CAFs (mCAF), including fibronectin 1 (*FN1*), lumican (*LUM*), and periostin (*POSTN*), were markedly elevated. The expression levels of markers associated with vascular CAFs (vCAF: *NOTCH3*, and *MCAM*), inflammatory CAFs (iCAF: *CXCL12*, *CCL2*, and *LIF*), and antigen-presenting CAFs (apCAF: *HLA-DRA*, *HLADRB1*, and *CD74*) remained unchanged. Remarkably, no significant differences in the expression of these CAF markers were observed between colorectal cancer and normal tissues (**Fig. 2B**). Additionally, we performed functional analyses on αSMA–positive CAFs and NFs from OCRC, colorectal cancer, and normal tissues. Kyoto Encyclopedia of Genes and Genomes and Gene Ontology enrichment analyses revealed that genes upregulated in CAFs from OCRC tissue are involved mainly in ECM–receptor interactions and the organization of extracellular structures. Interestingly, in colorectal cancer tissue, αSMA–positive CAFs were significantly enriched in genes involved in the degradation and catabolism of GAGs, indicating a functional divergence from OCRC CAFs (Supplementary Fig. S4A–S4C).

Furthermore, primary CAFs isolated from OCRC and colorectal cancer tissues were subjected to digital RNA-seq analysis. The results aligned with those from DSP, showing markedly increased expression levels of mCAF markers, *COL1A1*, *COL3A1*, *MMPs*, and *LOX* in CAFs derived from OCRC, whereas no significant changes were noted in the expression of markers for vCAFs, iCAFs, and apCAFs, and the functional analysis also revealed enrichment of the composition of the ECM (**Fig. 2C**; Supplementary Fig. S5A and S5B).

Finally, we conducted tissue multiplex immunofluorescence staining validation of OCRC and colorectal cancer samples and reported that the expression levels of αSMA, FN1, and POSTN and

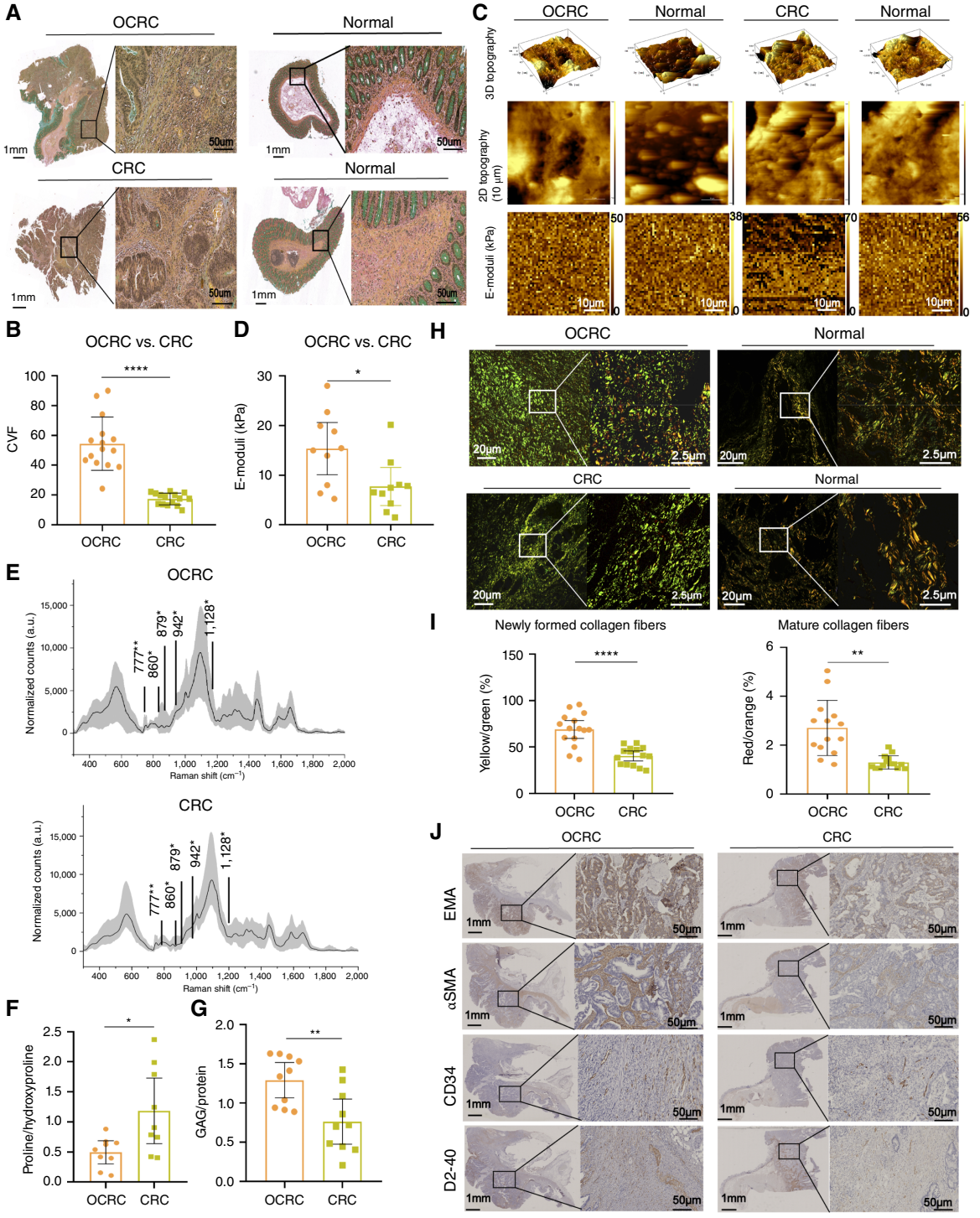

Figure 1.

OCRC and colorectal cancer differed substantially in ECM constitution, biomechanics, and collagen characteristics. **A,** Movat pentachrome staining of OCRC, colorectal cancer (CRC), and normal tissues. Scale bars, 1 mm and 50 μm. **B,** Analysis of collagen fiber content in OCRC and colorectal cancer tissues using Masson staining ($n = 15$). CVF, collagen volume fraction. **C,** Biomechanical evaluation of OCRC, colorectal cancer, and normal tissue by AFM. Scale bars, 10 μm. **D,** Mean E-moduli measured in OCRC and colorectal cancer tissues ($n = 10$). **E,** Raman spectroscopy analysis of the collagen fiber network in OCRC and colorectal cancer tissues ($n = 10$). **F** and **G,** Raman spectroscopy quantification analyzed the content of collagen and GAGs in the ECMs of OCRC and colorectal cancer tissues ($n = 10$). **H,** Structural analysis of collagen fibers in OCRC and colorectal cancer tissues by Picrosirius red staining and polarizing light microscopy. Scale bars, 20 and 2.5 μm. **I,** Quantification of newly formed collagen fibers and mature collagen fibers in OCRC and colorectal cancer tissues ($n = 15$). **J,** IHC staining analysis of the content of epithelial cells, CAFs, MVD, and MLD in the stroma of OCRC and colorectal cancer. Scale bars, 1 mm and 50 μm. Statistical significance was determined by an unpaired Student *t* test. *, $P < 0.05$; **, $P < 0.01$; ****, $P < 0.0001$.

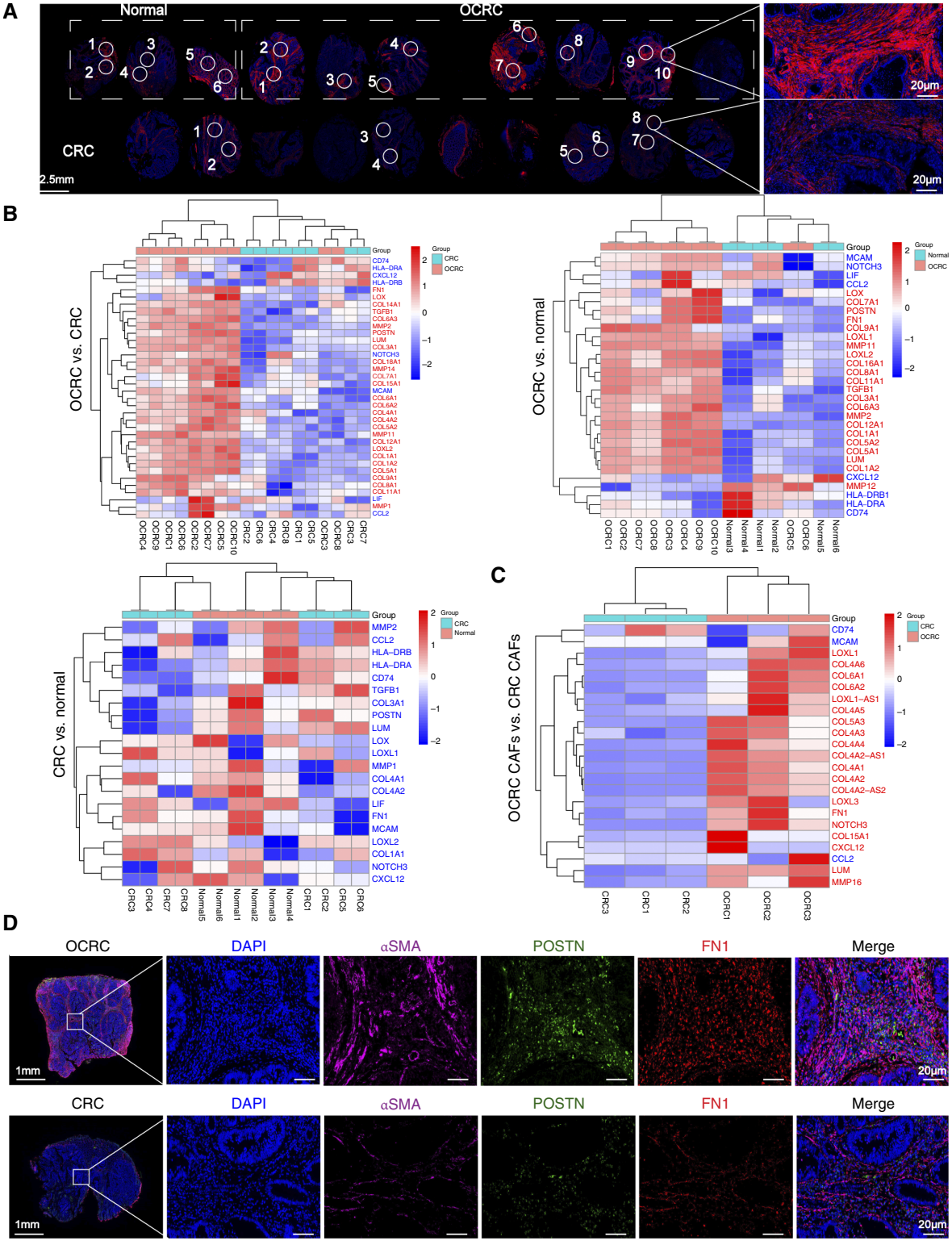

Figure 2.

OCRC and colorectal cancer differed in stromal cells, with significantly more matrix CAFs in OCRC. **A,** Quantitative analysis of OCRC, colorectal cancer (CRC), and normal tissues by DSP technology. Red, αSMA. Scale bars, 2.5 mm and 20 μm. **B,** Heatmap showing differential expression of marker genes associated with different CAF subtypes in OCRC, colorectal cancer, and normal tissues. **C,** Heatmap illustrating gene expression differences in CAFs derived from OCRC and colorectal cancer tissues. **D,** Tissue multiplex immunofluorescence staining analysis of OCRC and colorectal cancer tissues. Red, FN1; green, POSTN; purple, αSMA. Scale bars, 1 mm and 20 μm.

the ratio of FN1-positive CAFs were significantly elevated in OCRC tissue (**Fig. 2D**; Supplementary Fig. S3B and S3C). Moreover, we further verified by PCR and ELISA experiments that the expression of ECM-related matrix proteins (collagen I, collagen III, collagen IV, fibronectin, and LUM), MMPs (MMP1 and MMP3), LOX, and tissue inhibitor of MMP (TIMP1) in OCRC samples was significantly increased, whereas the expression of TIMP3 was decreased (Supplementary Fig. S5C and S5D). These results suggest that mCAFs are the predominant type of CAFs in OCRC and are critical for its pathogenesis.

OCRC- and colorectal cancer–derived CAFs exhibited significant functional differences

The role of the ECM in regulating cell adhesion, morphology, and viability is well known (25). Next, we experimentally validated these functional differences between the CAFs from the two groups. First, we examined the function of ECM-related protein secretion by CAFs. Compared with colorectal cancer–derived CAFs, OCRC-derived CAFs secreted significantly higher levels of collagen (types I, III, and IV), noncollagen proteins (laminin and fibronectin), and proteoglycans (HA). Similarly, because the composition and remodeling of the ECM are related to MMPs, we also measured the expression levels of related MMPs and the proteins that control MMP activity. The secretion of MMPs (MMP1, MMP2, MMP3, and MMP14), TIMP1, and LOX was notably greater in the OCRC group than in the control group, whereas the expression of TIMP3 was decreased (**Fig. 3A**; Supplementary Fig. S6A). These results also indicate that OCRC- and colorectal cancer–derived CAFs differ in their ECM-related protein secretion functions, that the ECM of OCRC may undergo significant remodeling, and that mCAFs constitute the main type of CAF in the OCRC matrix. Subsequently, we further examined the differences in tumor-promoting biological functions of CAFs derived from OCRC and colorectal cancer samples. We cocultured the CAF CM from each group with LoVo and SW480 cells to assess its influence on tumor progression (Supplementary Fig. S6B). Cell proliferation, migration, and invasion assays confirmed that OCRC-derived CAFs significantly enhanced the proliferation, migration, and invasion of colorectal cancer cells (Supplementary Fig. S6C–S6E). The 3D coculture assay revealed that OCRC-derived CAFs notably induced a spherical morphology and enhanced the metastatic potential of LoVo and SW480 cells (**Fig. 3B**). The OCRC CAF CM markedly promoted angiogenesis in HUVECs and EMT in colorectal cancer cells (**Fig. 3C** and **D**). Finally, through the construction of a colorectal cancer lung metastasis model, we found that CAFs derived from OCRC had a more significant effect on promoting colorectal cancer cell lung metastasis (**Fig. 3E**). Therefore, CAFs derived from OCRC showed more significant effects of promoting tumor progression, and this may explain why CAF levels, MVD, and the degree of EMT were higher in OCRC samples than in colorectal cancer samples. These findings demonstrate the heterogeneity and distinct biological functions of CAFs in OCRC and colorectal cancer tissues.

Changes in the physicochemical properties of the ECM are closely related to the interaction of cell functions in the TME. We found that the ECMs of OCRC and colorectal cancer samples differed in composition and that the biomechanics of the two were also significantly different. Tumor biomechanics have been recognized to be closely related to tumor progression and functional changes. Therefore, we further explored whether biomechanical changes in the ECM can positively affect CAF function. We applied FlexCell cyclic tensile strain to force (F) stimulation of OCRC- and colorectal cancer–derived CAFs (FOCRC and FCRC, respectively) and found that the secretion of matrix proteins, MMPs, LOX and TIMPs increased significantly in the ECMs in OCRC- and colorectal cancer–derived CAFs after force stimulation and that the ability to promote tumor progression was more significant (**Fig. 3**; Supplementary Fig. S6A–S6E). Moreover, our digital RNA-seq analysis of CAFs with or without force stimulation revealed that increased ECM biomechanics could positively activate the GAG biosynthesis function of CAFs, thereby accelerating ECM remodeling and tumor ECM development (Supplementary Fig. S6F). Therefore, elucidating the mechanisms underlying the differences in CAF abundance and functionality between OCRC and colorectal cancer samples is crucial for controlling the occurrence and progression of OCRC.

OCRC and colorectal cancer differed metabolically, with PA levels being elevated in OCRC

The BMI differed between patients with OCRC and those with colorectal cancer, and functional analysis of CAFs revealed enrichment of various metabolic pathways. We therefore compared metabolic function in OCRC and colorectal cancer samples via retrospective analysis of serum samples from 150 matched pairs of patients; the markers examined included triglycerides (TG), total cholesterol (CHOL), low-density lipoprotein CHOL (LDLC), high-density lipoprotein CHOL (HDLC), blood glucose, and the incidence of aortic atherosclerosis or calcification (AAS/AC) and coronary artery atherosclerosis or calcification (CAS/CAC). The OCRC group presented significantly elevated serum TG, CHOL, and LDLC levels and significantly lower HDLC levels, with no significant differences in blood glucose (Supplementary Fig. S7A). Patients with OCRC presented a greater incidence of AAS/AC and CAS/CAC, reinforcing the strong association between OCRC and dyslipidemia.

Further transcriptomic and untargeted metabolomic analyses of fresh tissue from five pairs of patients with OCRC and colorectal cancer revealed significant differences in fatty acid metabolism (Supplementary Fig. S7B). OCRC presented an elevated relative abundance of PA (Supplementary Fig. S7C). PA levels were significantly correlated with serum TG, CHOL, and HDLC levels, particularly in patients with OCRC, highlighting a significant association between OCRC occurrence and dyslipidemia, with notably elevated PA content in OCRC tissue (Supplementary Fig. S7D and S7E).

CAF content was associated with dyslipidemia and elevated intratumoral PA levels in OCRC

The lipid metabolism of patients with OCRC and colorectal cancer differed significantly, particularly with respect to PA in OCRC. OCRC and colorectal cancer samples differed in TME composition, including CAF and microvascular, microlymphatic, and epithelial cell levels, with notable functional differences in CAF ECM organization and metabolism (Supplementary Figs. S3, S4, and S5B). Consequently, we hypothesized that abnormal tumor metabolism in both groups may be associated with abnormalities in CAFs and other TME constituents. To verify this, we analyzed the correlations between the numbers of CAFs, epithelial cells, MVD, and MLD in OCRC and colorectal cancer tissues and the lipid parameters of the patients. These findings revealed a strong correlation between the number of CAFs in tumors and TG, CHOL, and LDLC levels, particularly in OCRC (Supplementary Fig. S8A). In contrast, the MVD, MLD, and number of epithelial cells were not significantly correlated with lipid levels (Supplementary Fig. S8B–S8D). These findings are consistent with the observed prevalences of AAS/

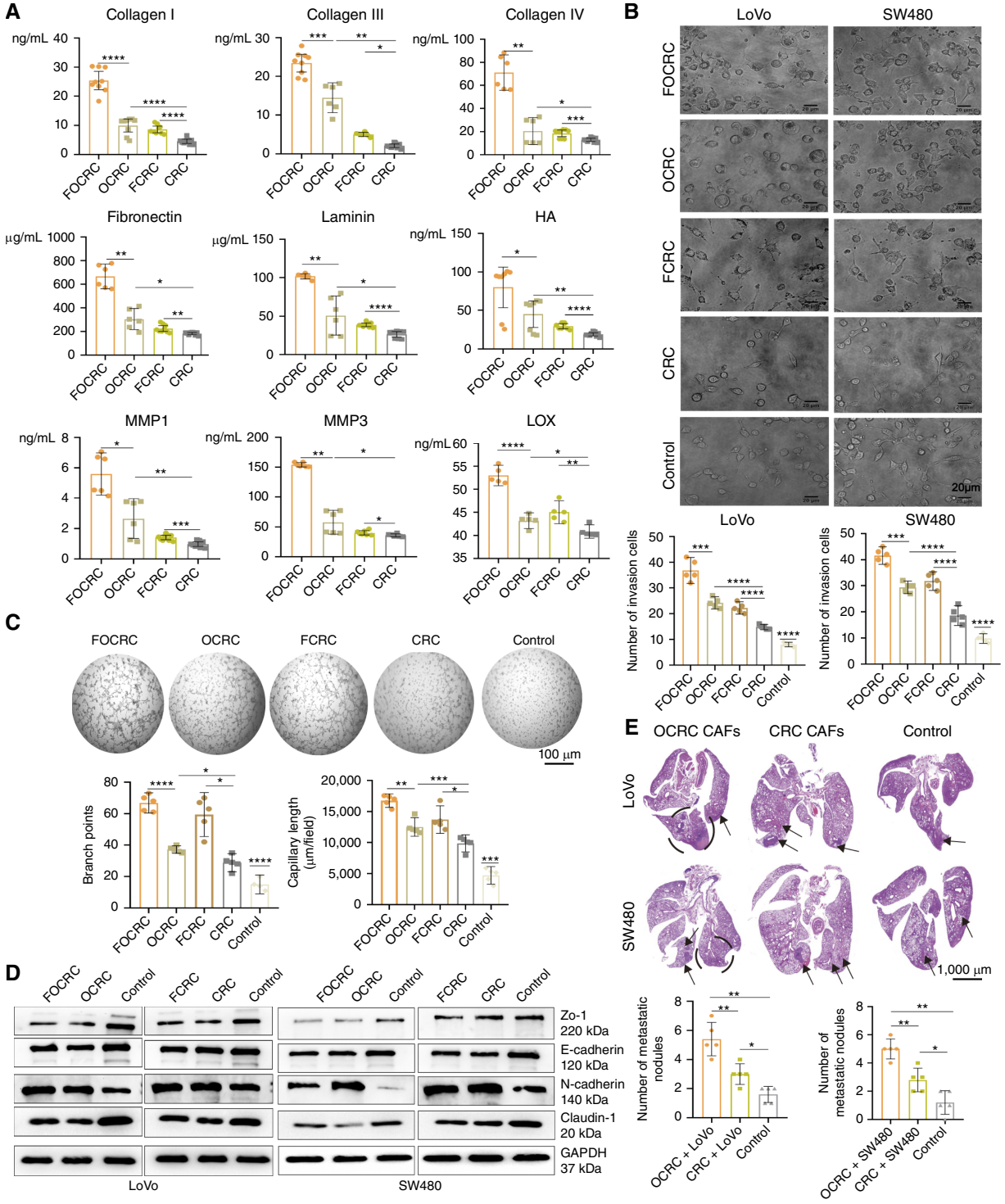

Figure 3.

OCRC- and colorectal cancer–derived CAFs exhibited significant functional differences. **A,** The function of ECM-related proteins, MMPs, LOX, and tissue inhibitor of MMP secretion by CAFs from OCRC and colorectal cancer (CRC) tissues ($n = 5$). **B,** Three-dimensional culture assays and semiquantitative analysis was performed to observe the effect of CAFs derived from OCRC and colorectal cancer on tumor cell invasion ($n = 5$). Scale bars, 20 μm. Colorectal cancer cells after CAF intervention extended protuberances to the Matrigel matrix, whereas control group cells formed tight spherical colonies. **C,** Angiogenesis assay using HUVECs treated with CM from OCRC- and colorectal cancer–derived CAFs. ($n = 5$). Scale bars, 100 μm. **D,** Analysis of EMT induction in colorectal cancer cells by CAFs derived from OCRC and colorectal cancer tissues. **E,** Promotion of colorectal cancer lung metastasis by CAFs derived from OCRC and colorectal cancer tissues. Statistical significance was determined by an unpaired Student *t* test. *, $P < 0.05$; **, $P < 0.01$; ***, $P < 0.001$; ****, $P < 0.0001$. FCRC, force-stimulated colorectal cancer–derived CAFs; FOCRC, force-stimulated OCRC-derived CAFs.

AC and CAS/CAC (Supplementary Fig. S9A). Therefore, changes in CAF content may be closely associated with abnormalities in lipid metabolism.

Given the elevated PA level in OCRC samples and its significant correlations with serum TG, CHOL, and LDLC levels in patients with OCRC (Supplementary Fig. S5), it is crucial to investigate whether the metabolic abnormalities that lead to increased intratumoral PA also substantially affect CAF content and function. We analyzed the correlations between the relative PA content in the tumors of both groups and the CAF, MVD, and MLD levels in the tumor tissue. As hypothesized, the relative content of PA was positively correlated with the CAF content and negatively correlated with epithelial cell number, particularly in OCRC tissues (Supplementary Fig. S9B). Moreover, mCAFs constitute the main component of the OCRC matrix (**Fig. 2**; Supplementary Fig. S3). Therefore, PA may be an important factor influencing CAF content and function. Clarifying the mechanisms underlying the relationship between PA and CAFs is crucial for controlling ECM remodeling and OCRC occurrence.

PA promoted CAF function and facilitated partial NF-to-mCAF activation

To verify whether elevated PA can promote CAF proliferation and functional conversion to mCAFs, we stimulated CAFs with different concentrations of PA (25, 50, or 100 μmol/L). Only at the highest concentration (100 μmol/L) did PA promote CAF proliferation, the secretion of ECM-related matrix proteins, LOX, MMPs and TIMPs, and the mRNA expression of *FN1*, *LUM*, and *POSTN*, whereas lower concentrations had no significant effect (**Fig. 4A**; Supplementary Fig. S10A–S10D). Although the highest concentration of PA increased CAF proliferation and secretory function, this finding does not fully explain the differences in ECM constitution and structure or the alterations in CAF content and function in OCRC tissue. Consequently, we wondered whether PA can directly stimulate NF proliferation and activate NF to CAF or mCAF. Western blotting, qPCR, and CCK-8 assays indicated that stimulation with different concentrations of PA neither induced the activation of NFs into CAFs and mCAFs nor promoted NF proliferation (Supplementary Fig. S10E–S10G). Therefore, PA may promote activation of NFs into CAFs following colorectal cancer cell stimulation. To test this hypothesis, we stimulated LoVo and SW480 cells with different concentrations of PA. Oil Red O staining revealed marked lipid deposition after 48 h of PA stimulation (Supplementary Fig. S11A and S11B). Subsequently, NFs were cocultured with PA-stimulated LoVo and SW480 cells to determine whether PA can promote the activation of NFs into CAFs. Immunofluorescence staining and Western blotting confirmed that NF expression of FAP and αSMA was significantly elevated (**Fig. 4B** and **C**). Both NF proliferation and the secretion of ECM-related matrix proteins, MMPs, LOX, and TIMPs increased with increasing PA concentration. Moreover, the protein and mRNA expression levels of the mCAF marker genes FN1, LUM, and POSTN were also increased (**Fig. 4A**; Supplementary Figs. S10C, S11C and S11D). Additionally, cellular multiplex immunofluorescence staining also confirmed that the number of FN1-positive CAFs was significantly increased, revealing that NFs can be partially activated into mCAFs (Supplementary Fig. S11E). Interestingly, the levels of secreted ECM-related matrix proteins, MMPs, and LOX were significantly greater following NF-to-CAF activation than following direct PA stimulation of CAFs, further indicating that PA can promote partial activation of NFs to mCAFs by stimulating colorectal cancer cells (Supplementary Fig. S11F).

Nonetheless, the mechanisms whereby PA regulates NF activation to CAFs remain unclear. PA can induce the secretion of colony stimulating factor 1 (CSF1), C-X-C motif chemokine ligand 8 (CXCL8), and TGFβ1 in hepatocellular carcinoma cells; these proteins are thought to promote the activation of macrophages and CAFs (26). To explore the mechanism by which PA regulates the activation of NFs into CAFs, transcriptomic sequencing analysis of SW480 cells after PA stimulation revealed that the expression levels of ECM-related matrix proteins (*COL3A1*, *MMP9*, and *TGFBI*), cytokines, and chemokines (*CCL2*, *CXCL8*, *TNF*, *CSF*, and *CXCL2*) were significantly increased. Kyoto Encyclopedia of Genes and Genomes and Gene Ontology enrichment analyses revealed that the upregulated differentially expressed genes were associated mainly with cytokine interactions and inflammatory pathways, and their functions were related mainly to cytokine activity, the ECM, and the chemokine response (Supplementary Fig. S12A–S12C). Therefore, we wondered whether PA is involved in promoting the activation of NFs to CAFs/mCAFs in colorectal cancer by regulating the secretion of CSF1, CXCL8, and TGFβ1 in tumor cells. Our qRT–PCR and ELISA results confirmed that PA stimulation of LoVo and SW480 cells promoted the mRNA and protein expression of CSF1, CXCL8, and TGFβ1 (**Fig. 4D**). CM was subsequently extracted from LoVo and SW480 cells stimulated with PA, and TGFβ1, CSF1, and CXCL8 inhibitors (ITD-1 (5 μmol/L), sotuletinib (0.5 μmol/L), and danirixin (12.5 nmol/L), respectively) were added and cocultured with NFs. The cellular multiplex immunofluorescence staining and Western blotting results revealed that the PA-induced activation of NFs into CAFs/mCAFs was significantly inhibited following this coculturing (**Fig. 4E** and **F**; Supplementary Fig. S12D). Therefore, PA both directly enhanced CAF function and stimulated activation of NFs to mCAFs by inducing colorectal cancer cells to secrete CSF1, TGFβ1, and CXCL8.

Dietary PA intervention promoted CAF activation, enhancing ECM stiffness and tumor proliferation

To investigate the biological effects of PA on colorectal cancer, we established two subcutaneous tumor models in C57BL/6 or BALB/c mice and an orthotopic tumor model in $Apc^{min/+}$ mice. All the mice were fed a diet containing 10% PA (with a total caloric intake equivalent to that of normal chow). The PA-fed mice presented significant increases in subcutaneous tumor volume and weight. Similarly, the orthotopic colorectal cancer model exhibited a notable increase in the number of tumors (**Fig. 5A**; Supplementary Fig. S13A). Following dietary PA intervention, intratumoral lipid deposition, PA, CAF, and collagen fiber contents were significantly elevated in both the subcutaneous and orthotopic tumors relative to those of controls. Biomechanical analysis of the ECM indicated that the tumor elastic modulus (E, $n = 3$) was markedly greater in the PA group than in the control group (**Fig. 5B–E**; Supplementary Fig. S13B–S13E). Interestingly, immunofluorescence staining analysis of subcutaneous and *in situ* tumor tissues revealed significantly elevated expression levels of αSMA and FN1 within the intratumoral matrix, with the proportion of FN1-positive CAFs increasing significantly after PA intervention (**Fig. 5F**; Supplementary Fig. S14A and S14B). These results further suggest that PA may increase the production of mCAFs.

Finally, we assessed whether PA can influence CSF1, CXCL8, and TGFβ1 secretion in the mice. Given the controversial nature of CXCL8 expression in mice, we instead measured the levels of CXCL1/KC. Serum and tumor tissue samples were collected from both groups. These results suggest increased serum and tumor levels

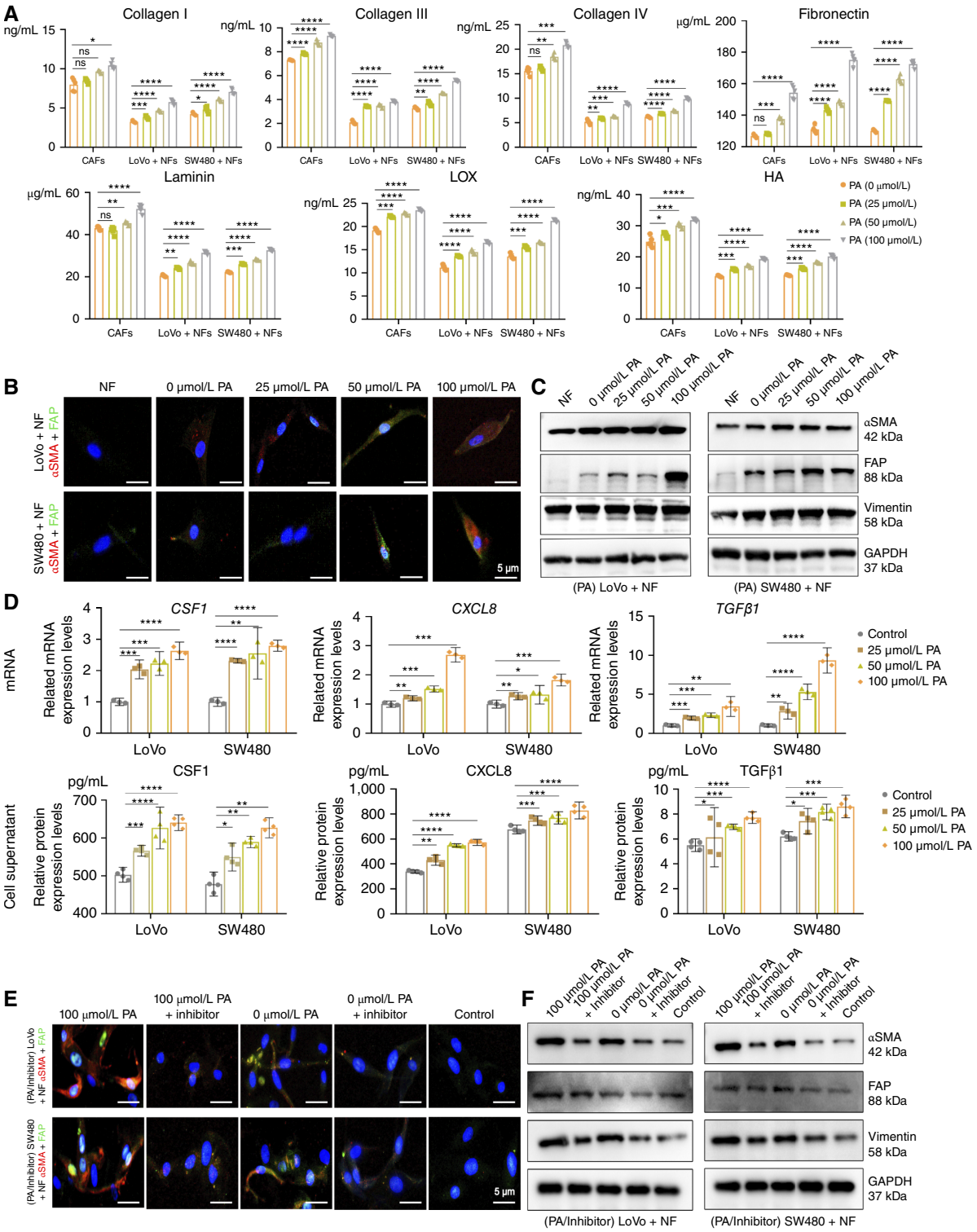

Figure 4.

PA promoted CAF function and facilitated partial NF-to-mCAF activation. **A,** Changes in ECM protein secretion function in CAF and NF following PA stimulation ($n = 5$). **B** and **C,** Cellular immunofluorescence staining (**B**) and Western blotting (**C**) verified that PA-stimulated colorectal cancer cells promote partial activation of NFs into CAFs. Scale bars, 5 μm. **D,** PA-induced alterations in mRNA and protein expression levels of CSF1, CXCL8, and TGFβ1 in LoVo and SW480 cells. **E** and **F,** Cellular immunofluorescence staining (**E**) and Western blotting (**F**) confirmed that neutralizing antibodies against CSF1, CXCL8, and TGFβ1 inhibit PA-mediated activation of NFs to CAFs. Scale bars, 5 μm. Statistical significance was determined by one-way ANOVA. *, $P < 0.05$; **, $P < 0.01$; ***, $P < 0.001$; ****, $P < 0.0001$; ns, not significant.

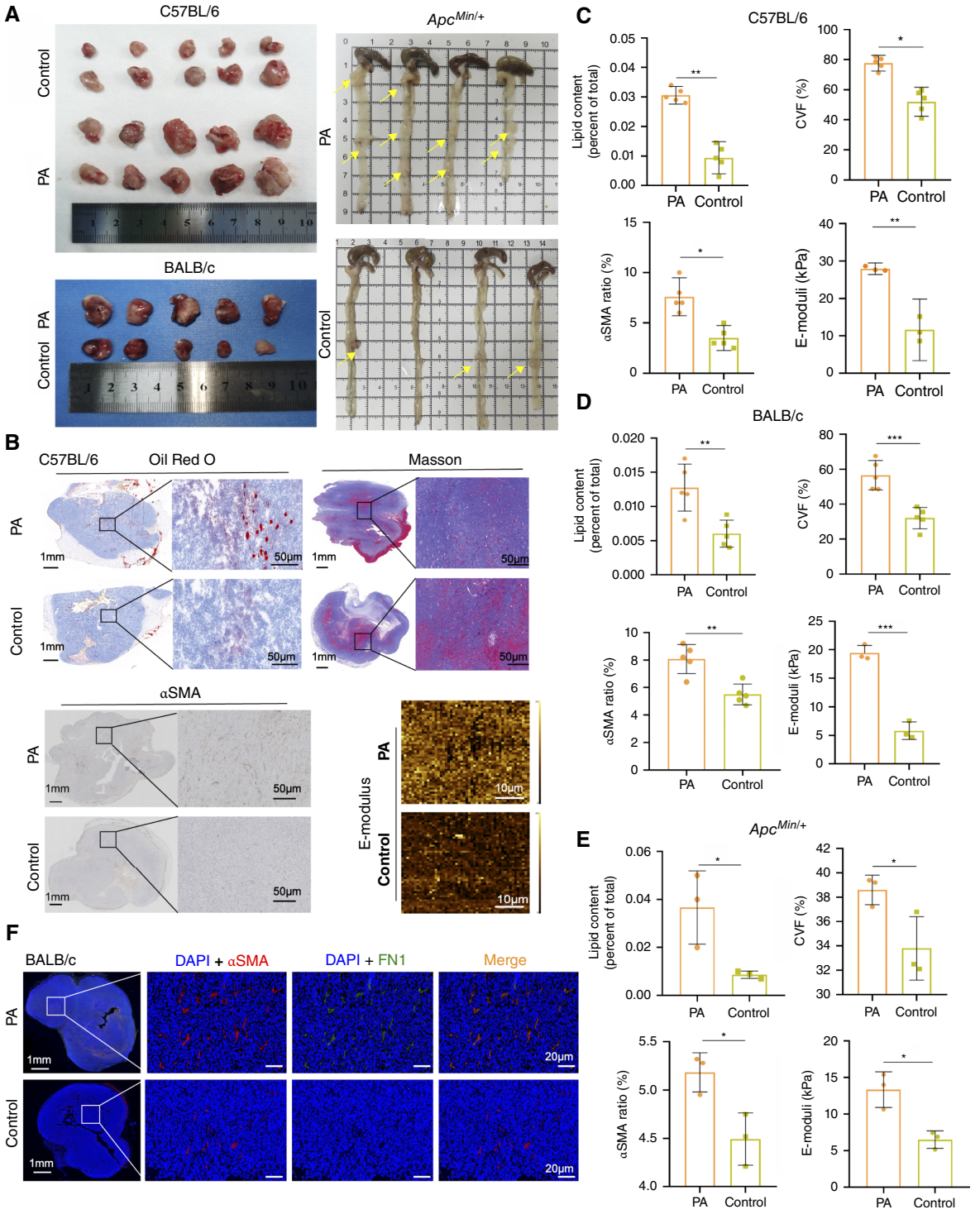

Figure 5.

Dietary PA intervention promoted CAF activation, enhancing ECM stiffness and tumor proliferation. **A,** Effects of PA-enriched high-fat diet on subcutaneous tumor growth in C57BL/6 ($n = 20$) and BALB/c mice ($n = 10$) and orthotopic tumors in $Apc^{min/+}$ mice ($n = 8$). **B,** Detection of lipid deposition, collagen fiber content, CAF abundance, and biomechanical properties in subcutaneous tumors of C57BL/6 mice. Scale bars, 1 mm and 50 μm; AFM, 10 μm. **C–E,** Semi-quantitative analysis of lipid deposition, collagen fiber content, CAF abundance, and biomechanical changes in ECM of subcutaneous and orthotopic CRC in C57BL/6 (**C**), BALB/c (**D**), and $Apc^{min/+}$ (**E**) mice models. **F,** Tissue immunofluorescence staining analysis of mCAFs in subcutaneous colorectal cancer of BALB/c mice. Green, FN1; red, αSMA. Scale bars, 1 mm and 20 μm. Statistical significance was determined by an unpaired Student *t* test. *, $P < 0.05$; **, $P < 0.01$; ***, $P < 0.001$. CVF, collagen volume fraction.

of CSF1, TGFβ1, and CXCL1/KC in the PA group (**Fig. 6A–C**). Therefore, using mouse subcutaneous and orthotopic colorectal cancer models, we confirmed that PA can regulate cytokine secretion in tumor cells, increasing CAF content in the TME and altering the physicochemical properties of the ECM, further promoting colorectal cancer progression.

PA enhanced fatty acid β-oxidation and protein kinase C activation in colorectal cancer cells, regulating cytokine secretion via the NF-κB pathway

Our *in vivo* and *in vitro* experiments revealed that PA enhanced CSF1, CXCL8, and TGFβ1 secretion in colorectal cancer cells. To elucidate the specific regulatory mechanisms involved, we conducted digital RNA-seq analysis of subcutaneous tumors ($n = 5$) from the two groups. These finding revealed that PA enhanced fatty acid oxidation in tumors (**Fig. 6D**), and consistent results were also obtained with tissue transcriptome sequencing and untargeted metabolomics analysis (Supplementary Fig. S5). Elevated levels of free fatty acids induce NF-κB activation via ROS generated by mitochondrial β-oxidation and accumulated diacylglycerol-activated protein kinase C (PKC), in turn regulating the secretion of several cytokines (27–29). Moreover, colorectal cancer cell transcriptome sequencing analysis revealed that differentially expressed genes were significantly enriched in the NF-κB signaling pathway after PA stimulation of SW480 cells (Supplementary Fig. S12B). Therefore, we hypothesized that PA regulates tumor cell CSF1, CXCL8, and TGFβ1 secretion via this pathway.

To test this hypothesis, we first examined whether the PA stimulation enhances reactive ROS production in colorectal cancer cells. The ROS levels increased proportionally to PA concentration (**Fig. 6E**). We next examined the association between PA stimulation and PKC activation. Western blotting revealed that PA significantly enhanced PKC phosphorylation in colorectal cancer cells (**Fig. 6F**). Consequently, we hypothesized that PA influences the secretion of CSF1, CXCL8, and TGFβ1 by colorectal cancer cells via the NF-κB pathway. To further elucidate the involvement of the NF-κB pathway, colorectal cancer cells were treated with 100 μmol/L PA and an NF-κB pathway inhibitor (QNZ, 160 nmol/L). Western blotting revealed a significant increase in the expression of phosphorylated IKK α/β, phosphorylated p65, TGFβ1, CSF1, and CXCL8 in LoVo and SW480 cells after PA stimulation, whereas the effects of PA were significantly attenuated by the addition of the inhibitor QNZ (**Fig. 6G**). ELISAs also confirmed that PA can promote the secretion of CSF1, TGFβ1, and CXCL8 in colorectal cancer cells and that this effect can be inhibited by QNZ (Supplementary Fig. S14C and S14D). Therefore, our findings support the hypothesis that PA influences CSF1, CXCL8, and TGFβ1 secretion in colorectal cancer cells primarily by activating the NF-κB pathway.

Vanillylacetone inhibited PA-induced CAF activation, ECM stiffness, and OCRC development

Various phytochemicals and natural products possess antioxidant, antitumor, and anti-inflammatory properties mediated by signaling pathways such as the Wnt/β-catenin, NF-κB, and MAPK, demonstrating significant therapeutic potential (30, 31). In this study, PA regulated cytokine secretion from colorectal cancer cells via the NF-κB pathway, thereby promoting the activation of CAFs and alterations in the ECM. To explore this further, we established a specialized natural chemical library (L2000-Z761734) aimed at inhibiting the NF-κB pathway in colorectal cancer to identify compounds that could inhibit CAF activation and ECM remodeling. Drug-screening identified the natural chemical compounds pyrogallol and vanillylacetone as inhibitors of PA stimulation–induced CSF1, CXCL8, and TGFβ1 secretion in colorectal cancer cells (**Fig. 7A**). Subsequent validation via qRT–PCR, Western blotting, and ELISA confirmed that vanillylacetone, but not pyrogallol, effectively inhibited PA-induced secretion of CSF1, CXCL8, and TGFβ1 in colorectal cancer cells by modulating the NF-κB pathway (**Fig. 7B**; Supplementary Fig. S15A–S15D).

To further validate the efficacy of vanillylacetone, we established two subcutaneous colorectal cancer models in C57BL/6 and BALB/c mice. The experimental group received a PA-containing diet (10% PA) and intraperitoneal injections of vanillylacetone (25 mg/kg). Posttreatment assessments revealed significant reductions in both tumor volume and weight in the vanillylacetone-treated group compared with the PA-fed and control groups, indicating that vanillylacetone effectively inhibited colorectal cancer progression (**Fig. 7C**; Supplementary Fig. S16A). The extent of ECM alteration, lipid deposition, CAF levels, collagen fiber content, and the ECM *E*-modulus were significantly lower in the vanillylacetone-treated mice than in the PA and control groups (**Fig. 7D** and **E**; Supplementary Fig. S16B and S16C). Intratumoral PA testing revealed that vanillylacetone treatment significantly reduced the increase in PA levels caused by the PA diet (Supplementary Fig. S16D). In addition, the intratumoral and serum CSF1, CXCL1/KC, and TGFβ1 levels were substantially lower in the vanillylacetone-treated group than in the PA-treated and control groups (Supplementary Fig. S17A and S17B). Additionally, tissue immunofluorescence staining revealed a decreased proportion of FN1-positive CAF cells in subcutaneous tumors treated with vanillylacetone, suggesting that vanillylacetone inhibits mCAF activation resulting from PA stimulation (**Fig. 7F**; Supplementary Fig. S17C and S17D). These preliminary findings indicate that vanillylacetone inhibits PA-induced mCAF activation, ECM stiffness, and OCRC development by suppressing cytokine secretion in colorectal cancer cells through NF-κB pathway. Interestingly, we found that the use of vanillylacetone in the control group of mice also inhibited tumor progression. Based on this observation, we propose that NF-κB, a common signaling pathway that promotes tumor progression, can be targeted by vanillylacetone to suppress tumor growth. Although the NF-κB is a common signaling pathway, in the TME with high PA levels, it serves as the primary route through which PA promotes ECM stiffness and the occurrence of OCRC. Identifying the main signaling pathways in different TMEs is crucial for controlling tumor progression.

Discussion

Patients with OCRC had a significantly poorer prognosis than patients with colorectal cancer in our cohort. The OCRC and colorectal cancer samples exhibited considerable differences in ECM constitution, with OCRC samples exhibiting greater CAF content and activity than colorectal cancer samples. Metabolically, OCRC and colorectal cancer samples differed significantly. PA, one of the most common fatty acids, accumulated in OCRC tissue, and its levels were highly correlated with the mCAF content. The fact that some of the patients with OCRC did not exhibit hyperlipidemia indicates that their PA accumulation was caused by abnormal lipid metabolism in colorectal cancer cells. Mechanistically, despite numerous regulatory mechanisms of tumor ECM remodeling, our multiomics analysis and experimental validation revealed that the pathway most significantly associated with PA accumulation–

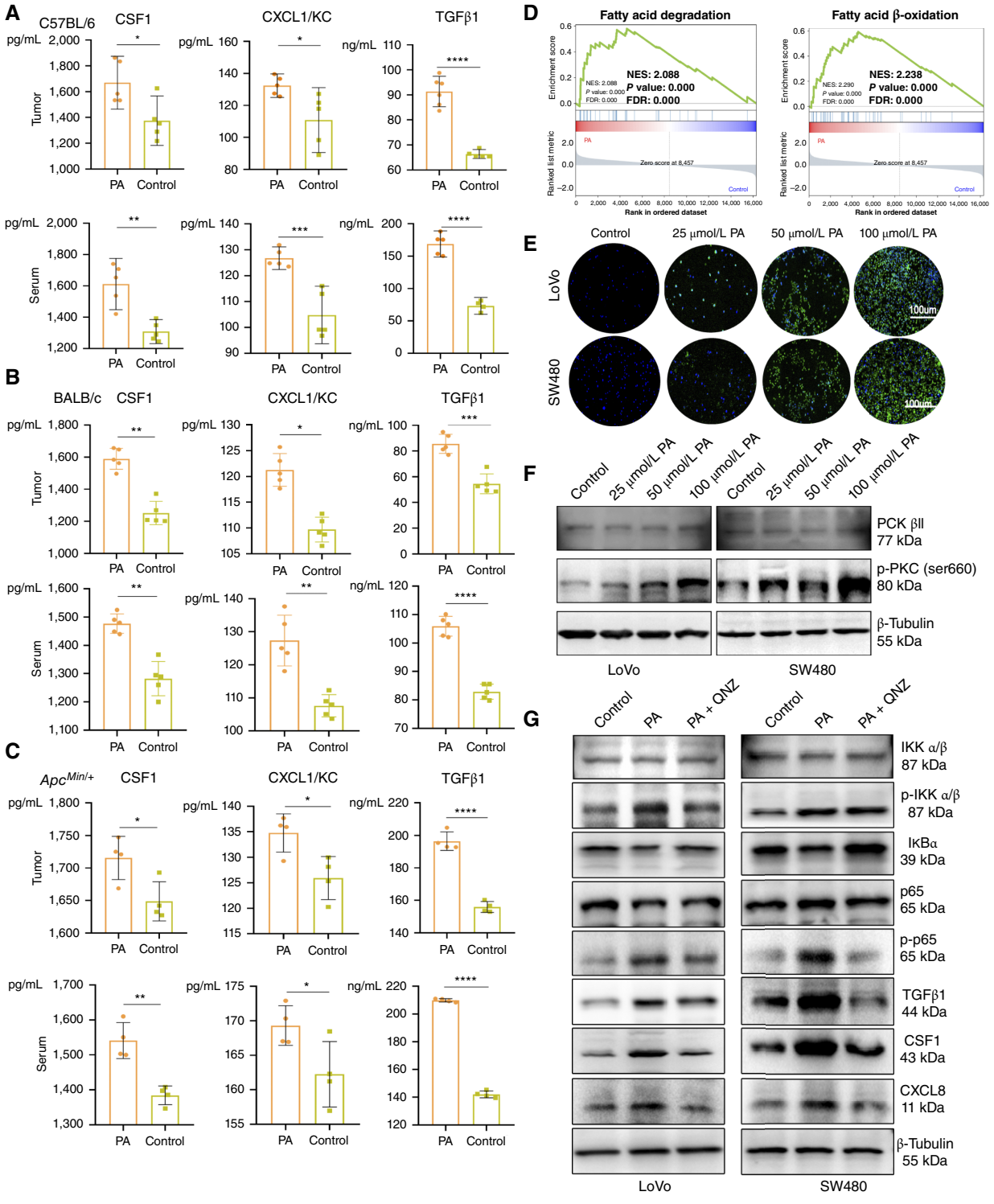

Figure 6.

PA enhanced fatty acid β-oxidation and protein kinase C activation in colorectal cancer cells, regulating cytokine secretion via the NF-κB pathway. **A–C,** Comparative analysis of CSF1, CXCL8, and TGFβ1 expression levels in subcutaneous and orthotopic tumors and serum in the PA and control groups. **D,** Enrichment analysis of gene set enrichment analysis pathway in subcutaneous tumors of PA-treated and control C57BL/6 mice ($n = 5$). NES, normalized enrichment score. **E,** ROS production in colorectal cancer cells following PA stimulation. Scale bars, 100 μm. **F,** Western blotting demonstrating enhanced phosphorylation PKC in colorectal cancer cells after PA intervention. **G,** Western blotting validation of PA-induced regulation of CSF1, CXCL8, and TGFβ1 secretion via the NF-κB pathway in colorectal cancer cells. Statistical significance was determined by an unpaired Student *t* test. *, $P < 0.05$; **, $P < 0.01$; ***, $P < 0.001$; ****, $P < 0.0001$.

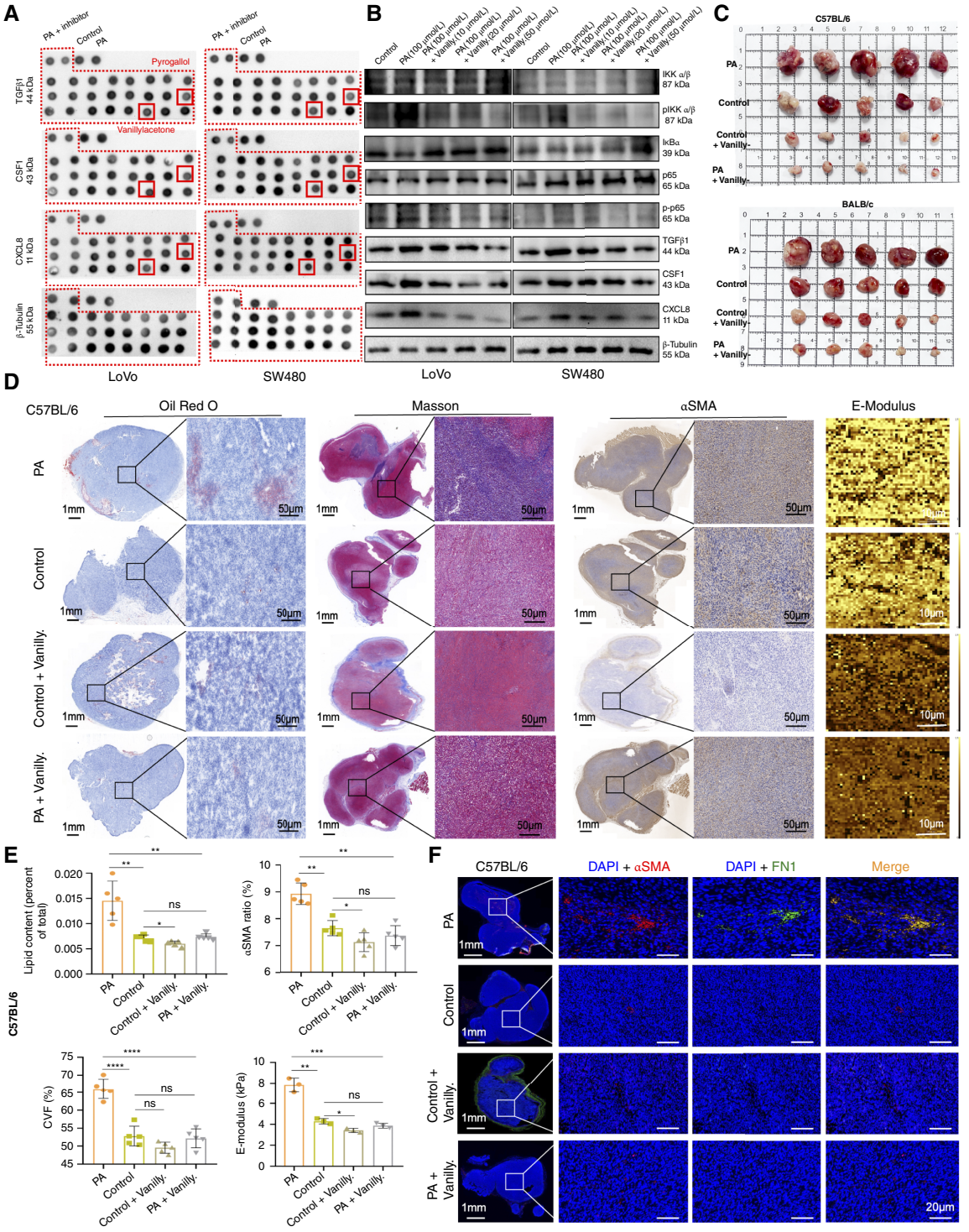

Figure 7.

Vanillylacetone inhibited PA-induced CAF activation, ECM stiffness, and OCRC development. **A,** Dot blot screening of potential therapeutic agents. **B,** Western blotting validates the efficacy of screened candidate agents. **C,** Antitumor efficacy of vanillylacetone in colorectal cancer subcutaneous tumor models in C57BL/6 ($n = 20$) and BALB/c mice ($n = 20$). **D** and **E,** Analysis of lipid deposition, collagen fiber content, CAF abundance, and biomechanical changes in the ECM of colorectal cancer subcutaneous tumors in C57BL/6 mice treated with vanillylacetone. Scale bars, 1 mm and 50 μm; AFM, 10 μm. **F,** Tissue immunofluorescence staining analysis of mCAFs in colorectal cancer subcutaneous tumors of C57BL/6 mice after vanillylacetone treatment. Green, FN1; red, αSMA. Scale bars, 1 mm and 50 μm. Statistical significance was determined by one-way and two-way ANOVA. **, $P < 0.01$; ***, $P < 0.001$; ****, $P < 0.0001$; ns, not significant. CVF, collagen volume fraction; Vanilly., vanillylacetone.

induced ECM stiffness was the NF-κB pathway. The use of QNZ significantly inhibited the biological effects of PA. Additionally, we discovered that the natural chemical vanillylacetone also affects the NF-κB pathway, inhibiting the biological effects of PA. Therefore, although the NF-κB pathway is a common cellular pathway, it can exhibit unexpected protumor effects in different tumor microenvironments. Elucidating the primary mechanisms occurring within various TMEs is highly important for controlling tumor progression.

Obstruction is a risk factor for poor prognosis in patients with colorectal cancer (32, 33). Consistent with this finding, OCRC exhibited a poorer prognosis in our study. Unfortunately, although various clinical modalities have been used to improve OCRC treatment, its prognosis has not been effectively improved and the underlying mechanisms remain unclear (34). Our results imply that targeting hyperlipidemia or PA accumulation may alleviate the risk of obstruction in OCRC and improve patient prognosis. Considering that an nonnegligible number of patients with colorectal cancer with *in situ* primary lesions experience colonic obstruction during preoperative therapy, further examination of the clinical effects of targeting PA accumulation is warranted.

OCRC is often considered a consequence of tumor progression, with colon cancer stages III and IV being more susceptible to obstruction than stages I and II owing to their larger tumor size and greater invasiveness. However, although our current findings indicate that there is no direct correlation between T stage and obstruction risk, we observed significant differences between OCRC and colorectal cancer in the constitution, structure, and biomechanics of the ECM. Therefore, OCRC may be associated with ECM alterations, which are closely associated with tumor development in various solid tumors (6–10). On the basis of our findings, changes in the ECM alter the biological function of colorectal cancer. Therefore, OCRC, a consequence of tumor progression, is likely to occur via a mechanism related to changes in the ECM.

Disorders in ECM homeostasis can cause novel cell–matrix interactions in the TME. CAFs, major producers of ECM and paracrine signals, play a significant role in regulating ECM remodeling and tumor progression, and changes in the physicochemical properties of the ECM can enhance CAF activation (9, 35, 36). In non–small cell lung cancer, CAFs can regulate tumor ECM stiffness and remodeling to promote cancer cell proliferation and metastasis (37). In a colorectal cancer liver metastasis model, increased liver stiffness triggered stellate-cell differentiation into myofibroblasts, thus promoting tumor progression (38). TGFβ release by pancreatic cancer cells induces CAFs to form adhesive ECM and activates myoblasts, promoting tumor progression (39). In this study, changes in CAF function altered ECM homeostasis, in turn promoting tumor progression and increasing the risk of OCRC. Therefore, differences in CAFs between OCRC and colorectal cancer may be crucial for ECM alterations and colonic obstructions. Consequently, the functional heterogeneity of CAFs and their role in OCRC and colorectal cancer warrant further study.

Our findings indicate that mCAFs constitute a principal component in OCRC, corroborating our earlier hypothesis centered on their primary roles in ECM remodeling. Additionally, mCAFs in OCRC have been found to facilitate tumor invasion, metastasis, angiogenesis, and the EMT process. Different types of CAFs are known to play distinct roles across various tumors. For example, iCAFs express hepatocyte growth factor to promote the progression of intrahepatic cholangiocarcinoma via MET, and myofibroblasts express hyaluronidase 2 to promote the progression of intrahepatic cholangiocarcinoma (40). In high-grade serous ovarian cancer, mCAFs express proteins such as αSMA and vimentin, promoting cancer progression through EMT mechanisms (41). vCAFs have been observed to secrete substantial amounts of IL6, inducing significant epigenetic modifications in cholangiocarcinoma cells, notably enhancing EZH2 expression, which furthers tumor progression (42). In pancreatic cancer, apCAFs specifically activate $CD4^+$ T cells and modulate tumor immunity (43). Given that ECM remodeling is a hallmark of OCRC, the influence of mCAFs is undeniable. Thus, targeting mCAFs for the diagnosis and therapeutic management of OCRC is a promising strategy.

The functional heterogeneity of CAFs in the TME may be associated with metabolic reprogramming, a hypoxic microenvironment, and their origin (44). In this study, OCRC samples presented substantial accumulation of PA, and PA levels were strongly correlated with mCAF content. Emerging evidence indicates that PA, as a signaling molecule, can regulate tumor progression via various pathways and that the affected pathway depends on differences in metabolic reprogramming among cancers (45). For example, in pancreatic cancer cells, PA activates the TLR4/ROS/NF-κB/MMP9 signaling pathway, thereby increasing tumor invasiveness (46). In liver cancer, PA induces cytokine secretion by tumor cells and promotes stromal cell activation, facilitating tumor progression (26). In this study, we demonstrated that PA activated CAFs and promoted the transformation of NFs into mCAFs, ultimately affecting ECM homeostasis and leading to the development of obstruction. This study provides the first systematic exploration of the potential mechanisms of interactions among between PA, NFs, and mCAFs in colorectal cancer. Notably, the natural compound vanillylacetone inhibited PA-induced ECM stiffness in colorectal cancer. Vanillylacetone, which is isolated from ginger plants, has numerous health benefits, including hypoglycemic, hypolipidemic, and anti-inflammatory effects (47–50). In our research, we found that vanillylacetone (25 mg/kg) inhibited the PA stimulation–induced secretion of CSF1, TGFβ1, and CXCL8 by colorectal cancer cells. Therefore, cancer progression, which may involve biological processes such as lipid metabolism and changes in CAF function, may be inhibited by vanillylacetone. The therapeutic potential of vanillylacetone against cancer should be urgently be examined, and novel combination therapies, with a particular focus on OCRC, should be developed.

There are several limitations to our study. First, although the concentration of PA in the *in vitro* experiment was calculated experimentally, there may still be some differences from the actual physiologic situation. In addition, there are differences between the actual obstructive type of colorectal cancer and the *in vivo* animal model of colorectal cancer that we constructed, which cannot completely simulate the occurrence and development of the entire OCRC. However, our study still has important clinical implications. In our study, clinical stiffness induced by PA, CAF content and OCRC were found to be closely related. We found that PA could regulate the secretion of colorectal cancer cytokines through the NF-κB pathway and promote the activation of NFs into CAFs/mCAFs and stiffness of the ECM. In addition, the biological effects of PA could be inhibited by vanillylacetone, which systematically reveals the potential mechanism of OCRC and provides new ideas for controlling the occurrence and development of OCRC.

These findings highlight the role of ECM stiffness in OCRC progression, suggesting that the clinical manifestation of obstruction may be a milestone in matrix-remodeling progression. OCRC provides an appropriate model for studying matrix remodeling, as it is clinically common and readily diagnosable,

with ECM stiffness notably correlated with poorer prognosis. In terms of ECM-remodeling mechanisms, the accumulation of PA in colorectal cancer cells primarily promotes the transformation of NFs into mCAFs via the NF-κB pathway, activating matrix remodeling and driving the development of obstruction and malignancy in colorectal cancer. These results provide a novel therapeutic strategy for patients with colorectal cancer, especially those at risk of obstruction.

Authors' Disclosures

No disclosures were reported.

Authors' Contributions

S. Deng: Conceptualization, data curation, funding acquisition, validation, investigation, methodology, writing–original draft. **J. Wang:** Data curation, formal analysis, methodology. **F. Zou:** Data curation, formal analysis, methodology. **D. Cheng:** Data curation, methodology. **M. Chen:** Methodology, writing–original draft. **J. Gu:** Data curation, validation. **J. Shi:** Resources, data curation. **J. Yang:** Resources, data curation. **Y. Xue:** Resources, data curation, validation. **Z. Jiang:** Resources, data curation. **L. Qin:** Data curation, formal analysis. **F. Mao:** Data curation, validation. **X. Chang:** Resources, data curation. **X. Nie:** Resources, data curation, validation. **L. Liu:** Resources, validation, methodology. **Y. Cao:** Resources, data curation, funding acquisition, writing–review and editing. **K. Cai:** Conceptualization, resources, funding acquisition, validation, visualization, project administration, writing–review and editing.

Acknowledgments

This study was supported by the 2021 Clinical Research Foundation of Wuhan Union Hospital (grant number F010620042200101506), China Postdoctoral Science Foundation (grant number 2024M751028), Hubei Key Laboratory of Biological Targeted Therapy, Union Hospital, Tongji Medical College, Huazhong University of Science and Technology (grant number 2022swbx008), Free Innovation Pre-Research Fund, Union Hospital, Tongji Medical College, Huazhong University of Science and Technology (grant number 2023XHYN027), and Natural Science Foundation of Hubei Province (grant number 2024AFB090). We thank YuceBio Technology Co., Ltd. (Shenzhen, China) for performing the DSP and data analysis.

Note

Supplementary data for this article are available at Cancer Research Online (http://cancerres.aacrjournals.org/).

Received August 12, 2024; revised November 27, 2024; accepted February 17, 2025; posted first February 24, 2025.

References

1. Siegel RL, Miller KD, Fuchs HE, Jemal A. Cancer statistics, 2021. CA Cancer J Clin 2021;71:7–33.
2. Gunnarsson H, Holm T, Ekholm A, Olsson L. Emergency presentation of colon cancer is most frequent during summer. Colorectal Dis 2011;13:663–8.
3. Furuke H, Komatsu S, Ikeda J, Tanaka S, Kumano T, Imura KI, et al. Self-expandable metallic stents contribute to reducing perioperative complications in colorectal cancer patients with acute obstruction. Anticancer Res 2018;38:1749–53.
4. Zorcolo L, Covotta L, Carlomagno N, Bartolo DCC. Safety of primary anastomosis in emergency colo-rectal surgery. Colorectal Dis 2003;5:262–9.
5. Okuda Y, Shimura T, Yamada T, Hirata Y, Yamaguchi R, Sakamoto E, et al. Colorectal obstruction is a potential prognostic factor for stage II colorectal cancer. Int J Clin Oncol 2018;23:1101–11.
6. Tian C, Clauser KR, Öhlund D, Rickelt S, Huang Y, Gupta M, et al. Proteomic analyses of ECM during pancreatic ductal adenocarcinoma progression reveal different contributions by tumor and stromal cells. Proc Natl Acad Sci U S A 2019;116:19609–18.
7. Yamauchi M, Gibbons DL, Zong C, Fradette JJ, Bota-Rabassedas N, Kurie JM. Fibroblast heterogeneity and its impact on extracellular matrix and immune landscape remodeling in cancer. Matrix Biol 2020;91–92:8–18.
8. Brauchle E, Kasper J, Daum R, Schierbaum N, Falch C, Kirschniak A, et al. Biomechanical and biomolecular characterization of extracellular matrix structures in human colon carcinomas. Matrix Biol 2018;68–69:180–93.
9. Levental KR, Yu H, Kass L, Lakins JN, Egeblad M, Erler JT, et al. Matrix crosslinking forces tumor progression by enhancing integrin signaling. Cell 2009;139:891–906.
10. Lopez JI, Kang I, You WK, McDonald DM, Weaver VM, et al. In situ force mapping of mammary gland transformation. Integr Biol (Camb) 2011;3:910–21.
11. Xu CJ, Mikami T, Nakamura T, Tsuruta T, Nakada N, Yanagisawa N, et al. Tumor budding, myofibroblast proliferation, and fibrosis in obstructing colon carcinoma: the roles of Hsp47 and basic fibroblast growth factor. Pathol Res Pract 2013;209:69–74.
12. Mao X, Xu J, Wang W, Liang C, Hua J, Liu J, et al. Crosstalk between cancer-associated fibroblasts and immune cells in the tumor microenvironment: new findings and future perspectives. Mol Cancer 2021;20:131.
13. Sleeboom JJF, van Tienderen GS, Schenke-Layland K, van der Laan LJW, Khalil AA, Verstegen MMA. The extracellular matrix as hallmark of cancer and metastasis: from biomechanics to therapeutic targets. Sci Transl Med 2024;16:eadg3840.
14. Hinderer S, Seifert J, Votteler M, Shen N, Rheinlaender J, Schäffer TE, et al. Engineering of a bio-functionalized hybrid off-the-shelf heart valve. Biomaterials 2014;35:2130–9.
15. Seifert J, Hammer CM, Rheinlaender J, Sel S, Scholz M, Paulsen F, et al. Distribution of Young's modulus in porcine corneas after riboflavin/UVA-induced collagen cross-linking as measured by atomic force microscopy. PLoS One 2014;9:e88186.
16. Cross SE, Jin YS, Rao J, Gimzewski JK. Nanomechanical analysis of cells from cancer patients. Nat Nanotechnol 2007;2:780–3.
17. Deng S, Cheng D, Wang J, Gu J, Xue Y, Jiang Z, et al. MYL9 expressed in cancer-associated fibroblasts regulate the immune microenvironment of colorectal cancer and promotes tumor progression in an autocrine manner. J Exp Clin Cancer Res 2023;42:294.
18. Van TM, Blank CU. A user's perspective on GeoMxTM digital spatial profiling. Immunooncol Technol 2019;1:11–8.
19. Votteler M, Carvajal Berrio DA, Pudlas M, Walles H, Stock UA, Schenke-Layland K. Raman spectroscopy for the non-contact and non-destructive monitoring of collagen damage within tissues. J Biophotonics 2012;5:47–56.
20. Pudlas M, Brauchle E, Klein TJ, Hutmacher DW, Schenke-Layland K. Non-invasive identification of proteoglycans and chondrocyte differentiation state by Raman microspectroscopy. J Biophotonics 2013;6:205–11.
21. Ellis R, Green E, Winlove CP. Structural analysis of glycosaminoglycans and proteoglycans by means of Raman microspectrometry. Connect Tissue Res 2009;50:29–36.
22. Najafi M, Farhood B, Mortezaee K. Extracellular matrix (ECM) stiffness and degradation as cancer drivers. J Cell Biochem 2019;120:2782–90.
23. Boeding JRE, Ramphal W, Crolla RMPH, Boonman-de Winter LJM, Gobardhan PD, Schreinemakers JMJ. Ileus caused by obstructing colorectal cancer-impact on long-term survival. Int J Colorectal Dis 2018;33:1393–400.
24. Pickup MW, Mouw JK, Weaver VM. The extracellular matrix modulates the hallmarks of cancer. EMBO Rep 2014;15:1243–53.
25. Rozario T, DeSimone DW. The extracellular matrix in development and morphogenesis: a dynamic view. Dev Biol 2010;341:126–40.
26. Murai H, Kodama T, Maesaka K, Tange S, Motooka D, Suzuki Y, et al. Multiomics identifies the link between intratumor steatosis and the exhausted tumor immune microenvironment in hepatocellular carcinoma. Hepatology 2023;77:77–91.
27. Senga S, Kobayashi N, Kawaguchi K, Ando A, Fujii H. Fatty acid-binding protein 5 (FABP5) promotes lipolysis of lipid droplets, de novo fatty acid (FA) synthesis and activation of nuclear factor-kappa B (NF-κB) signaling in cancer cells. Biochim Biophys Acta Mol Cell Biol Lipids 2018;1863:1057–67.
28. Zhang M, Liu ZZ, Aoshima K, Cai WL, Sun H, Xu T, et al. CECR2 drives breast cancer metastasis by promoting NF-κB signaling and macrophage-mediated immune suppression. Sci Transl Med 2022;14:eabf5473.

29. Korbecki J, Kojder K, Kapczuk P, Kupnicka P, Gawrońska-Szklarz B, Gutowska I, et al. The effect of hypoxia on the expression of CXC chemokines and CXC chemokine receptors-A review of literature. Int J Mol Sci 2021;22:843.
30. Liu Z, Wang K, Jiang C, Chen Y, Liu F, Xie M, et al. Morusin alleviates aortic valve calcification by inhibiting valve interstitial cell senescence through ccnd1/trim25/nrf2 axis. Adv Sci (Weinh) 2024;11:e2307319.
31. Xu H, Li L, Wang S, Wang Z, Qu L, Wang C, et al. Royal jelly acid suppresses hepatocellular carcinoma tumorigenicity by inhibiting H3 histone lactylation at H3K9la and H3K14la sites. Phytomedicine 2023;118:154940.
32. Atsushi I, Mitsuyoshi O, Kazuya Y, Syuhei K, Noriyuki K, Masashi M, et al. Long-term outcomes and prognostic factors of patients with obstructive colorectal cancer: a multicenter retrospective cohort study. World J Gastroenterol 2016;22:5237–45.
33. Yang Z, Wang L, Kang L, Xiang J, Peng j, Cui j, et al. Clinicopathologic characteristics and outcomes of patients with obstructive colorectal cancer. J Gastrointest Surg 2011;15:1213–22.
34. Muldoon RL. Malignant large bowel obstruction. Clin Colon Rectal Surg 2021; 34:251–61.
35. Yokota M, Kojima M, Higuchi Y, Nishizawa Y, Kobayashi A, Ito M, et al. Spread of tumor microenvironment contributes to colonic obstruction through subperitoneal fibroblast activation in colon cancer. Cancer Sci 2015;106:466–74.
36. Zeltz C, Primac I, Erusappan P, Alam J, Noel A, Gullberg D. Cancer-associated fibroblasts in desmoplastic tumors: emerging role of integrins. Semin Cancer Biol 2020;62:166–81.
37. Navab R, Strumpf D, To C, Pasko E, Kim KS, Park CJ, et al. Integrin α11β1 regulates cancer stromal stiffness and promotes tumorigenicity and metastasis in non-small cell lung cancer. Oncogene 2016;35:1899–908.
38. Dou C, Liu Z, Tu K, Zhang H, Chen C, Yaqoob U, et al. P300 acetyltransferase mediates stiffness-induced activation of hepatic stellate cells into tumor-promoting myofibroblasts. Gastroenterology 2018;154:2209–21.e14.
39. Khan Z, Marshall JF. The role of integrins in TGFβ activation in the tumour stroma. Cell Tissue Res 2016;365:657–73.
40. Affo S, Nair A, Brundu F, Ravichandra A, Bhattacharjee S, Matsuda M, et al. Promotion of cholangiocarcinoma growth by diverse cancer-associated fibroblast subpopulations. Cancer Cell 2021;39:866–82.e11.
41. Xu J, Fang Y, Chen K, Li S, Tang S, Ren Y, et al. Single-cell RNA sequencing reveals the tissue architecture in human high-grade serous ovarian cancer. Clin Cancer Res 2022;28:3590–602.
42. Zhang M, Yang H, Wan L, Wang Z, Wang H, Ge C, et al. Single-cell transcriptomic architecture and intercellular crosstalk of human intrahepatic cholangiocarcinoma. J Hepatol 2020;73:1118–30.
43. Elyada E, Bolisetty M, Laise P, Flynn WF, Courtois ET, Burkhart RA, et al. Cross-species single-cell analysis of pancreatic ductal adenocarcinoma reveals antigen-presenting cancer-associated fibroblasts. Cancer Discov 2019;9: 1102–23.
44. Fang Z, Meng Q, Xu J, Wang W, Zhang B, Liu J, et al. Signaling pathways in cancer-associated fibroblasts: recent advances and future perspectives. Cancer Commun (Lond) 2023;43:3–41.
45. Fatima S, Hu X, Gong RH, Huang C, Chen M, Wong HLX, et al. Palmitic acid is an intracellular signaling molecule involved in disease development. Cell Mol Life Sci 2019;76:2547–57.
46. Binker-Cosen MJ, Richards D, Oliver B, Gaisano HY, Binker MG, Cosen-Binker LI. Palmitic acid increases invasiveness of pancreatic cancer cells AsPC-1 through TLR4/ROS/NF-κB/MMP-9 signaling pathway. Biochem Biophys Res Commun 2017;484:152–8.
47. Al-Hashem FH, Bashir SO, Dawood AF, Aboonq MS, Bin-Jaliah I, Al-Garni AM, et al. Vanillylacetone attenuates cadmium chloride-induced hippocampal damage and memory loss through up-regulation of nuclear factor erythroid 2-related factor 2 gene and protein expression. Neural Regen Res 2024;19: 2750–9.
48. Zhu Y, Wang C, Luo J, Hua S, Li D, Peng L, et al. The protective role of Zingerone in a murine asthma model via activation of the AMPK/Nrf2/HO-1 pathway. Food Funct 2021;12:3120–31.
49. Alam MF, Hijri SI, Alshahrani S, Alqahtani SS, Jali AM, Ahmed RA, et al. Zingerone attenuates carfilzomib-induced cardiotoxicity in rats through oxidative stress and inflammatory cytokine network. Int J Mol Sci 2022;23:15617.
50. Kucukler S, Darendelioğlu E, Caglayan C, Ayna A, Yıldırım S, Kandemir FM. Zingerone attenuates vancomycin-induced hepatotoxicity in rats through regulation of oxidative stress, inflammation and apoptosis. Life Sci 2020;259: 118382.